

Review

Open Access



# Metal-organic framework-based self-supported electrodes for oxygen evolution reaction

Shulin Li<sup>1,2</sup>, Dai Tang<sup>3</sup>, Xiaofei Jing<sup>1,\*</sup>

<sup>1</sup>Key Laboratory of Polyoxometalate and Reticular Material Chemistry of Ministry of Education, Northeast Normal University, Changchun 130024, Jilin, China.

<sup>2</sup>School of Science and Engineering, The Chinese University of Hong Kong, Shenzhen 518172, Guangdong, China.

<sup>3</sup>School of Chemical and Biomolecular Engineering, Georgia Institute of Technology, Atlanta, GA 30332, USA.

\*Correspondence to: Dr. Xiaofei Jing, Key Laboratory of Polyoxometalate and Reticular Material Chemistry of Ministry of Education, Northeast Normal University, 5268 Renmin Street, Changchun 130024, Jilin, China. E-mail: jingxf100@nenu.edu.cn

**How to cite this article:** Li S, Tang D, Jing X. Metal-organic framework-based self-supported electrodes for oxygen evolution reaction. *Chem Synth* 2024;4:70. <https://dx.doi.org/10.20517/cs.2024.26>

**Received:** 28 Feb 2024 **First Decision:** 7 Apr 2024 **Revised:** 8 May 2024 **Accepted:** 24 May 2024 **Published:** 11 Nov 2024

**Academic Editor:** Ying Wan **Copy Editor:** Pei-Yun Wang **Production Editor:** Pei-Yun Wang

## Abstract

Oxygen evolution reactions (OER), commonly employed in applications such as metal-air batteries, water electrolysis, fuel cells, etc., often suffer from slow kinetics, thus leading to ultra-high potentials that severely affect device energy efficiency. Metal-organic frameworks (MOFs) have garnered massive attention as electrodes for OER, benefiting from their highly ordered porous frameworks, abundant accessible active metal sites, and adjustable lattice structures. However, using powdered MOFs in OER poses a challenge, limiting the exposure of numerous active sites and resulting in suboptimal efficiency. To address this limitation, the trend towards designing MOF-based self-supported electrodes with enhanced contact between MOFs and the current collector has gained considerable attention for OER applications. This review highlights recent advancements and future prospects in developing MOF-based self-supported electrodes for OER. We delve into various aspects, including preparation methods, optimization strategies, catalytic efficiencies, and OER mechanisms with MOF-based electrocatalysts. Furthermore, we explore the existing challenges associated with MOF-based self-supported electrodes for OER. This comprehensive overview provides valuable insights into the evolving landscape of MOF-based materials in advancing OER.

**Keywords:** Metal-organic frameworks (MOFs), electrocatalyst, self-supported electrodes, catalytic mechanism, oxygen evolution reaction (OER)



© The Author(s) 2024. **Open Access** This article is licensed under a Creative Commons Attribution 4.0 International License (<https://creativecommons.org/licenses/by/4.0/>), which permits unrestricted use, sharing, adaptation, distribution and reproduction in any medium or format, for any purpose, even commercially, as long as you give appropriate credit to the original author(s) and the source, provide a link to the Creative Commons license, and indicate if changes were made.



## INTRODUCTION

The escalating global demand for clean energy and the imperative to address environmental challenges underscore the urgency of developing sustainable energy sources<sup>[1,2]</sup>. Metal-air batteries, fuel cells, and water splitting technologies have garnered significant attention within the realm of emerging energy conversion and storage technologies due to their commendable efficiency, safety, and environmental consideration<sup>[3-6]</sup>. Despite their promising advantages, these technologies still encounter a critical challenge in oxygen evolution reactions (OER), the anodic half-reaction that necessitates substantial overpotentials due to its intricate multi-step, four-electron-proton transfer kinetics<sup>[7-11]</sup>. The reliance on catalysts based on precious metals, such as Pt, Ru, and Ir, has been proven to be effective but constrained by scarcity and high costs, prompting the exploration of non-precious metal-based catalysts such as Ni, Co, Fe, etc.<sup>[12-17]</sup>.

So far, various attempts have been at designing self-supported catalytic electrodes for direct application in OER. Hydroxide/oxyhydroxide, carbon-supported metal/oxide, oxide, sulfide, selenide, carbide, nitride, and phosphide electrode materials have been reported as self-supported inorganic electrodes<sup>[18-24]</sup>. In particular, the centers of OER catalytic activity are the metal sites bearing unsaturated coordination sites on the surfaces/interfaces and within defect structures of these electrode materials. Metal-organic frameworks (MOFs) represent a class of crystalline porous materials synthesized from metal nodes and organic linkers, garnering significant attention for their application in electrocatalysis<sup>[25-29]</sup>. Their well-defined structures, uniformly dispersed metal centers, and multi-dimensional periodic lattices have positioned them as desirable electrocatalysts for OER since 2016<sup>[30,31]</sup>. In particular, during the OER, the MOF surface undergoes remodeling to form metal hydroxides/oxyhydroxides, leading to abundant defects due to the porous structure and ligands in MOFs<sup>[32]</sup>. This makes MOF electrodes a promising kind of pre-OER electrocatalysts. However, a predominant drawback is the prevalent powder form of most MOFs, posing challenges related to low conductivity and stability, thereby impeding their progress<sup>[33,34]</sup>. To address this, including a polymer binder, such as Nafion, is a common practice to ensure strong adhesion to the conductive matrix during working electrode preparation<sup>[35]</sup>. However, introducing polymer linkers may induce sample aggregation, detrimentally affecting reactant adsorption, gas desorption processes, charge transfer efficiency, conductivity, and overall electrocatalytic activity<sup>[36]</sup>. To overcome these challenges, various preparation strategies, including *in situ* growth, scarified template, and electrochemical deposition, have been employed to tightly integrate MOFs onto conductive substrates, forming self-supported electrodes directly used as working electrodes. This approach simplifies the working electrode preparation process significantly. Compared to traditional powdered MOF catalysts, MOF-based self-supported electrodes not only facilitate accelerated charge and mass transport but also expose abundant active sites, thereby substantially enhancing catalytic performance<sup>[37-43]</sup>. Currently, diverse conductive substrates, such as metal foams<sup>[39,44]</sup>, carbon cloth (CC)<sup>[45]</sup>, and stainless-steel mesh<sup>[46,47]</sup>, are employed for fabricating MOF electrodes for OER. Additionally, exploring MOF-based self-supported electrodes exhibiting exceptional performance and stability at high current densities has led to their consideration as potential candidates for commercial electrolyzer electrodes<sup>[4,48-50]</sup>.

To enhance the OER performance of MOF-based self-supported electrodes, optimization strategies, including mixed-metal nodes, ligand design, and heterostructure engineering, have been embraced<sup>[51,52]</sup>. However, during the OER, MOF-based electrodes typically undergo surface or entire geometry and electron structure reconstruction due to factors such as electrolyte effects and applied electric fields. Therefore, it is essential to gain comprehensive insight into the *in situ* structural evolution and determination of the authentic active sites of electrocatalysts under practical reaction conditions<sup>[53]</sup>.

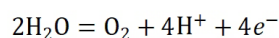


In energy conversion devices, the widespread evolution of MOF-based self-supported electrodes has showcased their unique advantages. Nevertheless, a comprehensive review focusing on the electrocatalytic OER application of these electrodes is currently lacking. This work addresses this gap by summarizing the progress in applying MOF-based self-supported electrodes for catalyzing OER. Initially, we present the fundamental principles and evaluation parameters of OER. Subsequently, we detail the preparation methods for MOF-based self-supported electrodes. Moving forward, we delve into the design principles and optimization strategies employed for enhancing the performance of these self-supported electrodes. Additionally, we propose *in situ* characterization technologies to elucidate the OER mechanism of pristine MOF electrodes. Further, we explore the application of various MOF-based self-supported electrodes in OER. In conclusion, we offer perspectives on efficient electrocatalytic OER by rationally constructing MOF-based self-supported electrodes.

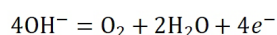
## MECHANISTIC UNDERSTANDING AND EVALUATION PARAMETERS OF OER

### OER mechanism

The OER entails the oxidation of water molecules ( $\text{H}_2\text{O}$ ) or hydroxyl ions ( $\text{OH}^-$ ) to generate oxygen ( $\text{O}_2$ ) through a four-proton/electron coupling process, ideally occurring near the thermodynamic limit of 1.23 V. Under acid conditions, the reaction is denoted as



While in alkaline solution, the reaction is expressed as



The OER mechanisms can follow three potential pathways: the adsorbent evolution mechanism (AEM), lattice oxygen mechanism (LOM), and oxidation pathway mechanism (OPM). AEM is widely acknowledged as the conventional OER mechanism, featuring a recognized scaling relationship among various reactions. According to the Sabatier principle, the reaction overpotential dominates by the binding strength of intermediates on catalyst surfaces. An overall understanding of the reaction mechanism and catalyst activity regulation, through experimental and theoretical observations, suggests that the involvement of lattice oxygen, denoted as LOM, may play an important role in the oxygen evolution. Compared to LOM, the OPM process is considered to be the ideal way to obtain direct O-O coupling. In addition, this review article focuses on OER under alkaline conditions.

### AEM

The AEM involves four proton-electron transfer reactions in active metal sites, as depicted in Figure 1A. First, to generate  $\cdot\text{OH}$ , the active sites must adsorb  $\text{OH}^-$  electrochemically and lose one electron. The adsorbed  $\cdot\text{OH}$  species is then deprotonated, which involves the synchronous removal of a proton and an electron, to produce  $\cdot\text{O}$  intermediate. Next, a second  $\text{OH}^-$  attacks the  $\cdot\text{O}$  species nucleophilically, transforming into  $\cdot\text{OOH}$ . Finally, the metal active site releases oxygen after further oxidation of  $\cdot\text{OOH}$ <sup>[54]</sup>. The AEM mechanism suggests that an effective OER catalyst should be able to absorb oxygen intermediates with the proper amount of energy. An ideal thermochemical catalyst should necessitate reaction free energies of comparable magnitudes for all four steps. However, catalysts deviate from this behavior due to the linear correlation between the adsorption energies of intermedia. According to the calculated scaling relationship from AEM, a catalyst requires at least a theoretical overpotential of 370 mV, which has been proven challenging to attain.

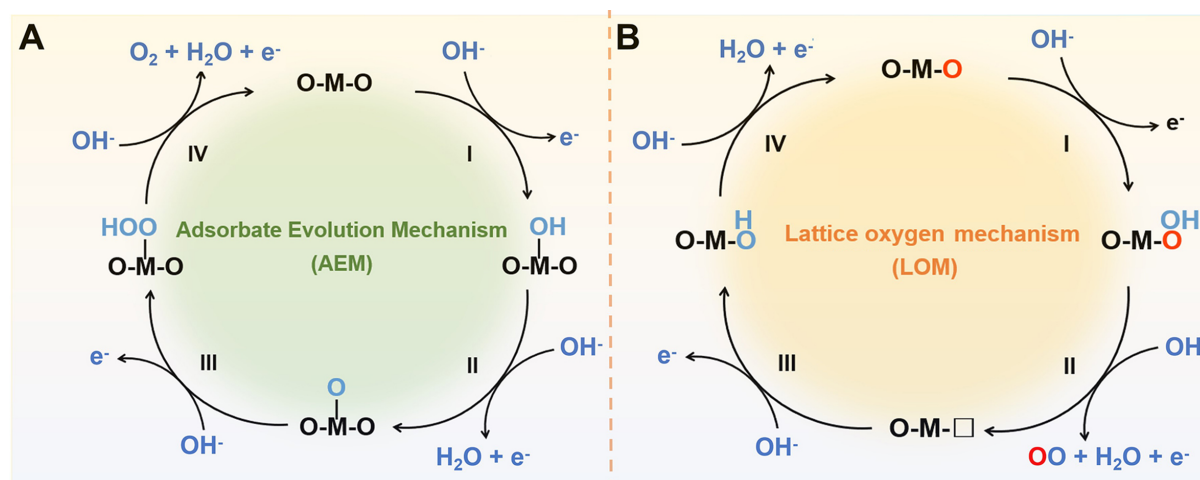


**Figure 1.** Schematic illustration of (A) AEM-based OER mechanism and (B) LOM-based OER mechanism. AEM: Adsorbate evolution mechanism; OER: oxygen evolution reaction; LOM: lattice oxygen mechanism.

### LOM

The evolution of more effective OER catalysts is foreseen by a new LOM route, as illustrated in Figure 1B. In contrast to the inactive lattice oxygen encountered in the AEM, the LOM mechanism activates it, engaging it in the OER process. First, lattice oxygen serves as the active site, turning into  $\cdot\text{OOH}$  intermediate upon interaction with  $\text{OH}^-$ . Oxygen is subsequently released after the second  $\text{OH}^-$  attack, simultaneously generating an oxygen vacancy. Following this,  $\text{OH}^-$  is adsorbed on the empty site to create  $\cdot\text{OH}$  species. Finally, a proton-electron transfer reaction restores the active site of lattice oxygen<sup>[55]</sup>. However, a drawback of this OER process is its potential to induce catalyst instability from a thermodynamic perspective, attributed to the involvement of lattice oxygen.

### OPM

OPM of homogeneous catalysts further improves OER performance through firsthand O-O radical coupling without oxygen vacancies or reaction intermediates ( $\cdot\text{OOH}$ )<sup>[56]</sup>. Here, we continue to focus on OPM in alkaline environments. In this process,  $\text{H}_2\text{O}/\text{OH}^-$  dissociates via the synergistic effect between the active metal sites, initiating driving O-O coupling and M-O radical coupling<sup>[57,58]</sup>. However, the symmetrical bimetallic sites with suitable atomic spacing are demanded in this mechanism to realize O-O radical coupling with a low energy barrier.

## Evaluation parameters

### Overpotential ( $\eta$ )

The overpotential ( $\eta$ ) is the difference between the thermodynamic equilibrium potential (1.23 V) of the reaction and the potential at which the catalyst is applied. The initial  $\eta$ , denoting the inherent activity of a catalyst, is commonly defined as the overpotential at the current density of  $1 \text{ mA}\cdot\text{cm}^{-2}$ , depending on the current density versus the potential plot<sup>[59]</sup>. Furthermore, the  $\eta$  value at a current density of  $10 \text{ mA}\cdot\text{cm}^{-2}$ , referred to as  $\eta_{10}$ , correlated with a photo-electrocatalytic water splitting efficiency of 12.3%, serving as a pivotal metric for evaluating electrocatalytic performance. Generally, lower overpotential signifies fewer reaction barriers to overcome and improved catalytic effect. However, for specific catalytic materials, such as Ni or Co-based compounds, notable redox peaks in the range may be slightly above the equilibrium potential. In such instances, the OER activity of the catalysts is evaluated using overpotentials at higher current densities of  $100 \text{ mA}\cdot\text{cm}^{-2}$ <sup>[60]</sup>.

### Tafel slope

The magnitude of the Tafel slope is a pivotal parameter for evaluating the electrocatalytic activity and is crucial in elucidating the catalytic mechanism of OER. In practice, attaining a desired current density often requires a disproportionately large overpotential. However, the overall goal is to minimize this overpotential and expedite the increase of current density. The Tafel equation below fits the linear part of Tafel plot, computing Tafel slope ( $b$ ) that quantifies the rate of current increase concerning overpotential:

$$\eta = a + b \times \log j \quad (1)$$

where  $b$  represents Tafel slope,  $j$  denotes current density,  $\eta$  stands for overpotential, and  $a$  is a constant determined by electrolyte, temperature, and electrode properties. The rate of current density change along with electrode potential can be represented by Tafel slope. Generally, a lower Tafel slope corresponds to swifter electron migration and heightened catalytic activity. Except for catalytic activity, Tafel slope can also rationally interpret the reaction mechanism by demonstrating the rate-determining step (RDS) of OER. The exchange current density ( $j^0$ ) of the electrocatalyst, denoting the abscissa of the intersection of two curves, is determined by extrapolating the linear Tafel area of anode/cathode polarization<sup>[61]</sup>. A high-quality OER electrocatalyst typically manifests a low Tafel slope and a high  $j^0$  value.

### Turnover frequency

The turnover frequency (TOF) is critical for assessing the inherent property of an electrocatalyst at a specified overpotential. The measurement quantifies the ratio of production normalization based on the amount of active sites and is computed using

$$TOF = \frac{jN_A}{nF\Gamma} \quad (2)$$

where  $N_A$  is the Avogadro constant,  $n$  stands for the number of electrons that migrate during a redox reaction at a specific  $\eta$ ,  $F$  is the Faraday constant, and  $\Gamma$  is the concentrated active sites, either on the surface or in total<sup>[5]</sup>.

In practice, the determination of TOF values is prone to variability due to frequent overestimation in the active site calculations. A pragmatic approach for estimating TOF values of OER from  $3d$  transition metal of electrocatalysts involves integrating the redox peak area for converting oxide/hydroxide to oxyhydroxide. Only the metal sites as active sites directly participate in the *in situ* redox reaction, aiming to provide a more accurate assessment.

### Faradaic efficiency

Faradaic efficiency (FE) serves as a crucial metric in assessing the charge transfer efficiency and selectivity of a catalyst, providing insights into whether undesired reactions accompany the desired reaction<sup>[62]</sup>. Meanwhile, FE signifies the efficiency of hydrogen or oxygen generation through electron conversion. For OER, a FE value is the ratio of oxygen produced through practical to theoretical values. Gas chromatography (GC) is employed to quantify actual oxygen generation, while chronoamperometric analysis determines the theoretical yield of oxygen. A superb OER electrocatalyst typically attains a FE close to 100% FE.

### Electrochemically active surface areas

Electrochemically active surface areas (ECSA) allow for analysis of the actual surface area exposed to the electrolyte involved. They serve as a core evaluation measure for the electrocatalytic performance of OER

catalysts, exhibiting a positive correlation with the double layer capacitor ( $C_{dl}$ ).  $C_{dl}$  is typically based on cyclic voltammetry (CV) curves at various scanning speeds in the non-faradaic area<sup>[63]</sup>. The evaluation method for ESCA and its corresponding results relies on electrochemical reactions and materials, making it challenging to serve as a precise metric for comparing different electrocatalysts across diverse conditions. In contrast, ESCA proves valuable for evaluating the performance of a set of similar materials under identical conditions.

#### *Electrochemical impedance spectroscopy*

Electrochemical impedance spectroscopy (EIS) analysis is an effective method for evaluating the catalytic kinetics of electrocatalysts and exploring electrode/electrolyte interface properties. EIS measurements are conducted over a voltage range of 10 mV below the system open-circuit voltage and a frequency range of  $10^5$  to 0.1 or 0.01 Hz. In the EIS spectrum, the high-frequency range reflects the rapid movement of electrons on the conducting material and ions in the electrolyte, while the mid- or low-frequency ranges represent the electrochemical reactions on the surface of the working electrode. The charge transfer resistance ( $R_{ct}$ ) is determined by fitting the semicircular diameter of the high-frequency region, which directly reflects the interfacial charge transfer at the electrode. A lower  $R_{ct}$  value indicates a faster response. It is important to note that  $R_{ct}$  values may be affected by the applied voltage. Therefore, measurements and comparisons of impedance spectra for the same group of materials should be made at consistent potential.

#### *Mass and specific activity*

The catalytic performance of an electrocatalyst is assessed by both mass and specific activity<sup>[5,64]</sup>. Mass activity specifically denotes the current standardized to the mass loading of the electrocatalyst at a designated overpotential. High mass activity implies achieving significant catalytic performance while using a minimal amount of electrocatalyst, making it a pertinent metric for cost-effectiveness. In contrast, non-precious metal-based electrocatalysts downplay the significance of mass activity. Specific activity, on the other hand, is typically normalized by factors such as the Brunauer-Emmett-Teller (BET) surface area or ECSA of electrode surface area. Among these parameters, ECSA, with its widespread applicability, is deemed the most suitable for capturing the inherent catalytic properties of the electrocatalyst.

#### *Stability*

It is imperative to prioritize stability performance when evaluating catalysts for practical applications. Various methods have been employed to characterize this aspect. The accelerated durability test represents one such approach, wherein the material's linear sweep voltammetry (LSV) curve is scrutinized pre- and post-exposure to CV cycles (> 1,000 cycles) at an elevated scan rate. A catalyst demonstrating heightened stability manifests a minimal shift in the overpotential of the benchmark current density ( $\eta_{10}$ ). Another methodology involves scrutinizing the long-operated chronopotentiometry curve ( $E-t$  curve at constant current) or the chronoamperometry curve ( $I-t$  curve at constant potential). A subtle rise in overpotential observed in the chronopotentiometry curve or a negligible reduction in current density in the chronoamperometry curve signifies the catalyst's robust stability when subjected to testing for a minimum of 12 h.

## PREPARATION STRATEGY OF MOF-BASED SELF-SUPPORTED ELECTRODES

Diverse strategies have been devised to prepare MOF-based self-supported electrodes. This paper delineates three prominent methodologies: *in situ* preparation strategy, template preparation strategy, and electrochemical deposition. These approaches hinge on the selection of substrates and the inherent structure of MOFs.

### ***In situ* preparation strategy**

Benefiting from its broad applicability and superior efficiency, *in situ* preparation of MOFs on diverse conductive substrates is progressively emerging as a ubiquitous method for preparing MOF-based self-supported electrodes<sup>[65-69]</sup>. Briefly, a pre-treated substrate is sequentially immersed in a solution containing metal ions and organic ligands; then, under hydrothermal/solvothermal conditions, a thin MOF film on the substrate is formed. Nickel foam (NF), characterized by a 3D macroporous structure and high electrical conductivity, is commonly chosen as the substrate for MOF growth<sup>[70,71]</sup>. Pioneering work by Zhao *et al.* in 2016 identified a MOF-based self-supported electrode with outstanding OER catalytic performance<sup>[31]</sup>. Specifically, the construction of this electrode involved the *in situ* preparation of 2,6-naphthalenedicarboxylic acid dipotassium as an organic ligand grown on NF [Figure 2A]. The resulting film, comprising an array of vertically grown MOF nanosheets on NF, exhibited well-defined morphology and rich porosity [Figure 2B]. The optimized NiFe-MOF self-supported electrode demonstrated good OER performance, achieving a minimal overpotential of 240 mV at 10 mA·cm<sup>-2</sup> and a Tafel slope of 34 mV·dec<sup>-1</sup> [Figure 2C]. Additionally, the water-stable NH<sub>2</sub>-Material of Institute Lavoisier (MIL)-88B(Fe<sub>2</sub>Ni)-MOF via *in situ* grown on NF was designed by Senthil Raja *et al.*, as a high-efficiency bifunctional electrode for overall water splitting with exceptional stability at high current densities [Figure 2D]<sup>[72]</sup>. Similarly, Wang *et al.* prepared novel 2D FeNi-based bimetallic MOF nanoarrays using thiophenedicarboxylate acid (H<sub>2</sub> TDC) as organic linkers on NF through an *in situ* strategy [Figure 2E]<sup>[73]</sup>. In addition to NF, other conductive substrates, such as copper foam (CF), copper foil, CC, *etc.*, were also employed. Li *et al.* developed an oriented nanosheet array film of 3D MOF M<sub>2</sub>(BDC)<sub>2</sub>TED (M = Co, Ni and Co/Ni; BDC = 1,4-benzenedicarboxylate; TED = triethylenediamine) on CF and copper foil, respectively. The integrated MOF-based self-supported electrode exhibited good OER performance, achieving current densities of 10 and 50 mA·cm<sup>-2</sup> at the overpotentials of 260 and 287 mV, with a Tafel slope of 76.24 mV·dec<sup>-1</sup>. Furthermore, it demonstrates faster electron transfer and high electrochemical stability in 1.0 M KOH aqueous solution<sup>[74]</sup>.

### **Template preparation strategy**

Compared to the *in situ* growth method, the template preparation strategy offers a more straightforward approach to prepare MOF films with well-defined morphology and structure, particularly enabling the growth of challenging 3D MOF films directly on conductive substrates. This technique is categorized based on the degree of template sacrifice, distinguishing between the semi-sacrifice and the full-sacrifice template methods<sup>[75-77]</sup>. In the semi-sacrifice template approach, the conductive substrate, such as metal foam, screen mesh, *etc.*, acts as a semi-sacrificial template. During the growth of MOF film, these substrates act as the sole metal sources, undergoing partial dissolution. Cao *et al.* reported the preparation of a self-supported 2D MOF nanocomposite electrode using NiFe alloy foam (NFF) to function as both the exclusive metal source and substrate [Figure 3A]<sup>[78]</sup>. The ultrathin Ni-rich Ni(Fe)-MOF nanosheet, with a thickness of approximately 1.56 nm, featured uniform Fe(Ni)-MOF clusters ranging from 2-5 nm in particle size [Figure 3B]. This self-supported MOF-based electrode, serving directly as the working electrode, exhibited outstanding OER activity with an overpotential of 227 mV for  $\eta_{10}$  and a Tafel slope of 38.9 mV·dec<sup>-1</sup>. In a separated study, Zhong *et al.* prepared serial Material of Institut Lavoisier (MIL)-53 self-supported electrodes through a mild one-step approach, utilizing recycled stainless steel as a semi-sacrifice template [Figure 3C]<sup>[47]</sup>. The waste stainless-steel matrix (SSM), acting as both the metal source and substrate, was chosen to coordinate with the organic ligand (benzene-1,4-dicarboxylic acid, H<sub>2</sub>BDC). This approach can orthotopically construct a MOF/substrate material in the simple and continuous solvothermal conditions.

It is well established that transition metal hydroxides, characterized by diverse compositions and structures, exhibit superior uniform growth on conductive substrate surfaces compared to MOFs. Leveraging these advantages, using self-supported metal hydroxide electrodes, also acting as templates (semi-sacrifice or full-sacrifice template), proves effective in regulating MOF growth<sup>[79]</sup>. This approach enhances MOF-substrate



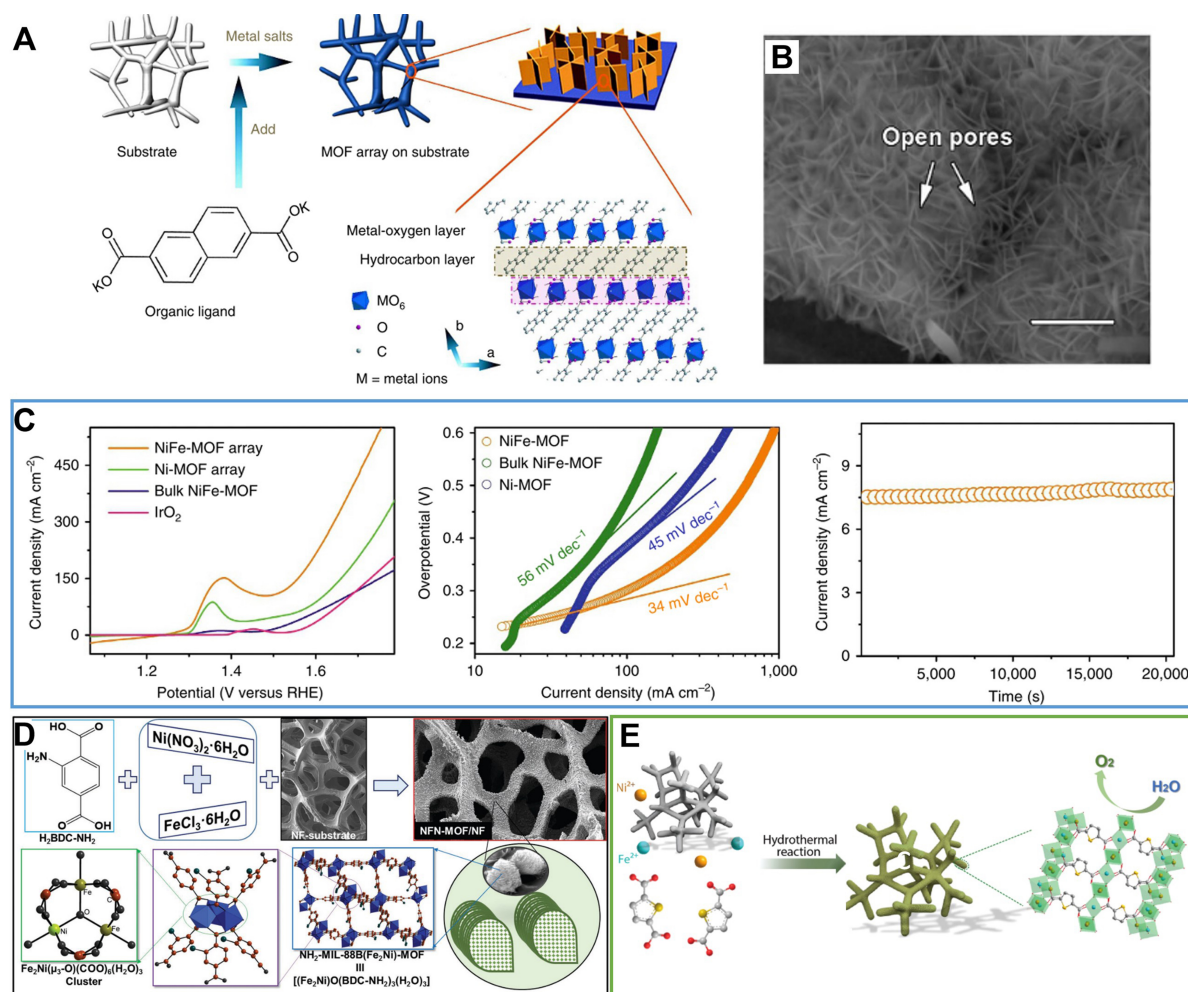


**Figure 2.** (A) Synthetic process of MOF nanosheet array; (B) SEM image for NiFe-MOF nanosheet; (C) Electrocatalytic properties of NiFe-MOF and other samples for OER. (A)–(C) were reproduced with permission<sup>[41]</sup>. Copyright 2017, Nature Publishing Group; (D) Schematic illustration of synthetic process for *in situ* growth of microbundles of NH<sub>2</sub>-MIL-88B(Fe<sub>2</sub>Ni)-MOF nanosheets on NF, reproduced with permission<sup>[72]</sup>. Copyright 2018, Wiley-VCH; (E) Schematic illustration of the synthesis of FeNi-MOF nanoarrays via a hydrothermal method, reproduced with permission<sup>[73]</sup>. Copyright 2021, American Chemical Society. MOF: Metal-organic framework; SEM: scanning electron microscope; OER: oxygen evolution reaction; MIL: material of Institut Lavoisier; NF: nickel foam.

interaction, creating varied electrode morphologies and structures. Our group employed a semi-sacrificial template strategy to obtain 3D ionic NiFe-MOF films by *in situ* growth, utilizing 1,4-bis(4H-1,2,4-triazol-4-yl)benzene (btz) as a neutral azolate ligand [Figure 4A]<sup>[80,81]</sup>. A uniform layer of nanosheet Ni(OH)<sub>2</sub> grown on NF releases metal ions, facilitating the formation of 3D MOF films through the extensive intergrowth of MOF particles under solvothermal conditions [Figure 4B and C]. The resulting 3D NiFe-MOF with great OER performance had a low overpotential of 239 mV at  $\eta_{10}$  and a low Tafel slope of 44.3 mV·dec<sup>-1</sup> in 1 M KOH electrolyte [Figure 4D and E]. Wang *et al.* utilized a CC substrate to synthesize a conductive MOF (cMOF)/layered double hydroxide (LDH) heteronanotube array, comprising lattice-matched 2D cMOF [Ni/Co-hexahydroxytriphenylene (HHTP)] and trimetallic CoNiFeLDH nanowires [Figure 4F]<sup>[45]</sup>. CoNiFe-LDH nanowires on NF served as an interior semi-sacrifice template, enabling grafting growth for cMOF/LDH heterostructures along LDH nanowires. The resulting cMOF/LDH/CC showed ultra-high intrinsic activity and mass transport for OER in alkaline conditions, attributed to enhanced conductivity of the cMOF shell, induced catalytic synergy at the heterojunctions in the CoNiFe-LDH core and rich active sites



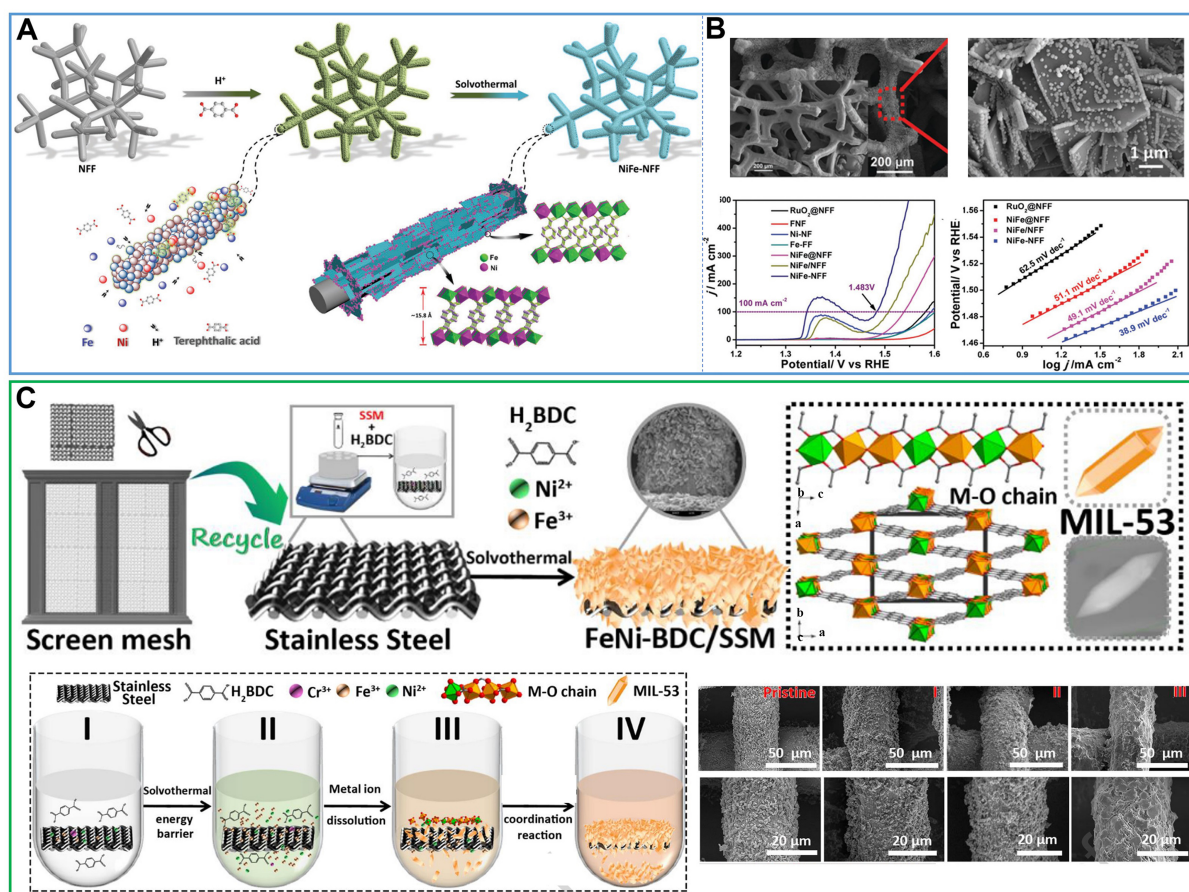


**Figure 3.** (A) Schematic representation for the formation of NiFe-NFF electrode and (B) SEM images and electrocatalytic properties of NiFe-NFF electrode and other samples for OER. (A) and (B) were reproduced with permission<sup>[78]</sup>. Copyright 2019, Wiley-VCH; (C) Schematic diagram for the growth of FeNiBDC/SSM composite (Step I-IV), reproduced with permission<sup>[47]</sup>. Copyright 2022, Elsevier. NFF: NiFe alloy foam; SEM: scanning electron microscope; OER: oxygen evolution reaction; BDC: 1,4-benzenedicarboxylate; SSM: stainless-steel matrix.

[Figure 4G and H]. In contrast to heterojunction formation, the full-sacrifice template strategy preserves only the unique morphology of the template. Cheng *et al.* grew hierarchical NiMn-MOF nanosheets built with a 2,6-naphthalenedicarboxyl acid ligand on multi-channel carbon fibers (MCCF/NiMn-MOFs) using a full-sacrifice template strategy, including the uniform NiMn LDH synthesis and ligand exchange procedure<sup>[82]</sup>. Owing to the etching of H<sup>+</sup> chelation of naphthalenedicarboxyl groups, these NiMn-LDH nanosheets were *in situ* completely converted into NiMn-MOF nanosheets in this exchange process. The as-prepared MCCF/NiMn-MOFs delivered 10 mA·cm<sup>-2</sup> at the overpotential of 280 mV and exhibited a Tafel slope of 85 mV·dec<sup>-1</sup> and good electrochemistry stability. Preparation of inorganic compounds by hydrolysis of soluble metal salts in near-neutral or alkaline media (hydrolysis products have weak physical bonds with the metal matrix). Wang *et al.* proposed a new organic acid etching (AES) strategy based on the idea that acids can oxidize metals to ensure the sustained release of metal cations<sup>[53]</sup>. Using  $\pi$ -conjugated ferrocene (Fc) dicarboxylic acid as an etchant and organic ligand, serial MFC-MOF (M = Ni, Co, Fe, Zn) nanosheets were prepared on metal frameworks.

While various template methods have been explored for synthesizing MOF-based self-supported electrodes, pursuing simpler and more economical strategies is imperative for designing and fabricating high-performance electrodes tailored to efficient electrochemical processes.

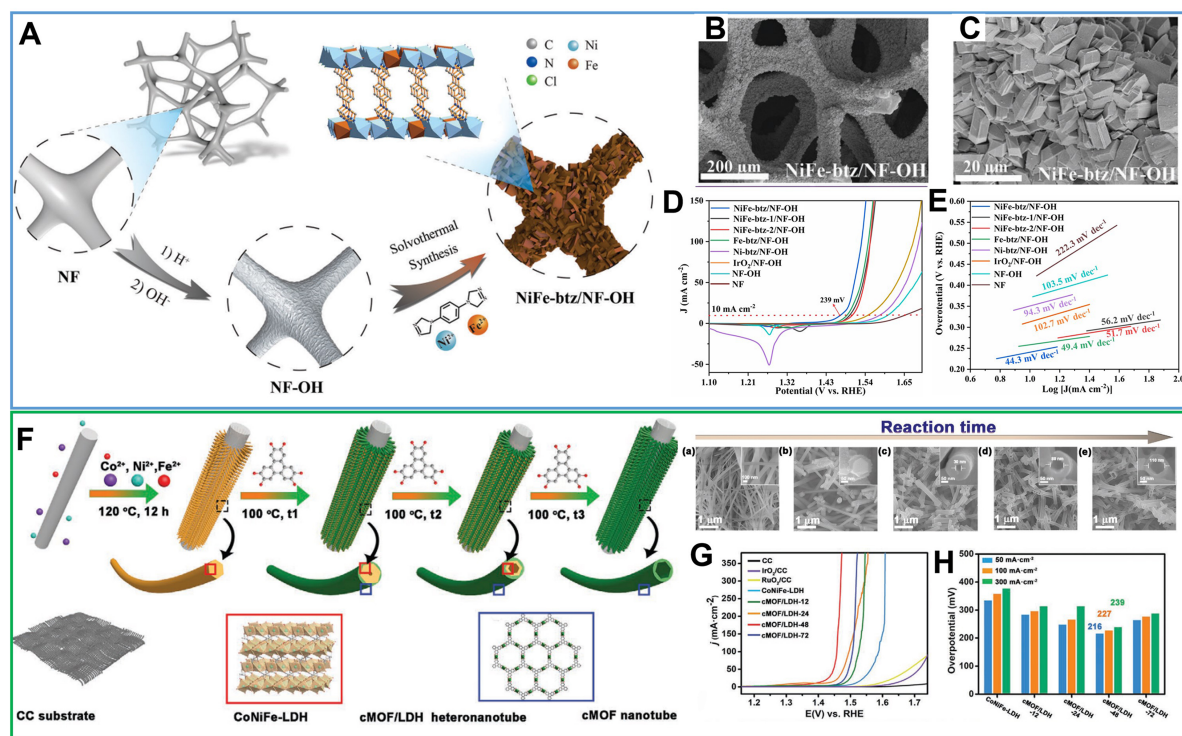


**Figure 4.** (A) Illustration of the fabrication route of NiFe-btz/NF-OH electrode; (B) and (C) SEM images for NiFe-btz/NF-OH electrode; (D) and (E) Electrochemical properties of NiFe-btz/NF-OH and other samples for OER. (A)-(E) were reproduced with permission<sup>[80]</sup>. Copyright 2022, Wiley-VCH; (F) Schematic illustration for constructing hierarchical porous MOF/LDH heteronanotube array electrode on CC substrate with prolonged reaction times. (a) SEM images of CoNiFe-LDH template, (b-e) SEM images of cMOF and cMOF/LDH obtained from 12, 24, 48, and 72 h reactions; (G) LSV curves of CoNiFe-LDH template and cMOF/LDH heteronanotube arrays; (H) Comparison for overpotentials of CoNiFe-LDH and cMOF/LDH heteronanotube arrays; (F)-(H) were reproduced with permission<sup>[45]</sup>. Copyright 2021, Wiley-VCH. btz: 1,4-bis(4H-1,2,4-triazol-4-yl)benzene; SEM: scanning electron microscope; OER: oxygen evolution reaction; cMOF: conductive metal-organic framework; LDH: layered double hydroxide; CC: carbon cloth; LSV: linear sweep voltammetry.

## Electrochemical deposition

Electrochemical deposition stands out as an elegant method due to its efficiency in achieving time-saving, milder, and controllable conditions for directionally growing thin films on a substrate, in contrast to conventional approaches such as *in situ* and template preparation strategies, which require relatively harsh synthesis conditions<sup>[83-86]</sup>. The electrochemical deposition approach encompasses three distinct types, referred to as anodic electrodeposition (AED), cathodic electrodeposition (CED), and electrophoretic deposition (EPD). AED and CED facilitate the *in situ* preparation of MOFs on substrate, while EPD involves depositing pre-synthesized MOFs. In the AED process, electrodes, such as metal foams, meshes, or foils, are impregnated in a solvent containing electrolytes and organic ligands, followed by the application of an anodic voltage. This generates the metal oxidation, releasing metal ions that interact with the organic ligands in the solvent, resulting in the deposition of a well-adhered thin film of MOF on the electrode. Conversely, CED, by applying a cathode potential, allows the preparation of continuous and dense MOF film electrodes. For instance, using NF as a substrate, Wang *et al.* deprotonated 1,3,5-benzenetricarboxylic acid (BTC) by applying a negative voltage of -1.5 V; the dissociative  $\text{H}^+$  ions absorbed electrons to produce hydrogen. The deprotonated  $\text{BTC}^{3-}$  eventually reacted with  $\text{Ni}^{2+}$  and  $\text{Fe}^{3+}$  ions to acquire a bimetallic MOF film on the NF surface<sup>[87]</sup>. The Fe/Ni MOF film exhibited good electrocatalytic performance, featuring an overpotential of 270 mV at 10  $\text{mA cm}^{-2}$ , a small Tafel slope of 47  $\text{mV dec}^{-1}$ , and remarkable stability. The CED method enables the control over metal type in the electrolyte, facilitating the preparation of layer-by-layer assembled polymetallic MOF film electrodes. For instance, Shahbazi Farahani *et al.* prepared

trimetallic MOF film electrode using layer-by-layer (LbL) assembly through a reductive electrochemical deposition strategy, where metal cations in each layer or at the interface of two layers are connected by bridging 2-amino-1, 4-phenyldicarboxylic acid linker<sup>[88]</sup>. The resulting Fe-Co-Ni MOF film, with single-phase, three-layer Fe-Co-Ni MOF film, maintains highly crystalline, fractionated porosity and chemical stability, enhancing active site accessibility and mass transport. This trimetallic Fe-Co-Ni MOF film electrode demonstrated exceptional performance, achieving low overpotentials of 254 mV for a current density of 10 mA·cm<sup>-2</sup> during OER in 1 M KOH.

In addition, an electrochemical approach allows the integration of MOF and graphene electrodes for enhanced OER performance. Lyu *et al.* have heightened the catalytic properties of MOFs through nanoconfinement of graphene multilayers [Figure 5A]<sup>[89]</sup>. The fabrication of MOF/graphene electrodes employed a two-electrode electrochemical system. Briefly, commercial graphite foil underwent treatment in 0.5 M H<sub>2</sub>SO<sub>4</sub> solution for 0.5 h to yield graphite multilayers. Subsequently, a specific organic salt solution served as an electrolyte, facilitating the insertion of organic ligands into the immersed ink layer. The treated graphite electrode was immersed in a metal salt solution, leading to MOF intercalation at the interface of the graphite multilayer. This nanoconfinement reduces the overpotential of electrochemical reactions and refines the electronic structure and catalytic center of MOF materials [Figure 5B]. The as-prepared MOF/graphene electrode attains 10 mA·cm<sup>-2</sup> with an ultralow overpotential of 106 mV and superb stability over 150 h for OER [Figure 5C-E].

In summary, MOF-based self-supported electrodes are predominantly composed of metal foam (e.g., Ni foam), with a smaller proportion of carbon-based materials (e.g., fiber papers and CC) and stainless-steel mesh. Different preparation methods will be used depending on the rated properties of substrate materials. The direct *in situ* growth strategy generally applies to all of the above substrates. However, unlike carbon-based materials, NF and stainless-steel mesh can act as sacrificial templates themselves, which will result in stronger interaction between MOF films and substrates. In addition, stainless-steel mesh substrates are more commonly used in the industry due to their high mechanical strength, flexibility, lower cost, and simpler production process compared to other conductive substrates. Therefore, MOF-based self-supported electrode preparation should also adopt a more moderate substrate and synthesis routes to large-scale preparation of large-area electrodes upon industrial demand.

## OPTIMIZATION APPROACH OF MOF-BASED SELF-SUPPORTED ELECTRODES

Optimization approaches, including mixed-metal nodes engineering, ligands design, amorphous engineering and heterostructure engineering, hold the potential to augment exposed active sites and enhance the intrinsic catalytic activity, thus advancing the OER performance of MOF-based electrodes [Table 1]. However, the majority of MOF electrodes experience surface geometry alteration, electronic structure reconstruction, or even complete structure transformations during the OER process, induced by electrolyte effects and applied electric field. Therefore, attaining an in-depth comprehension of *in situ* structural evolution of MOF electrodes and discerning the authentic active site under practical conditions emerges as a pivotal factor for the judicious design and optimization of electrodes endowed with favorable catalytic properties.

### Mixed-metal nodes

The majority of research shows that catalytic active sites for OER in pristine MOF electrodes primarily originate from unsaturated metal coordination sites. The introduction of heterogeneous metal centers may be a viable strategy to generate strong interfacial electronic effects, promote charge transport, change the electronic structure and optimize electronic orbitals, which, in turn, optimizes the binding energy of the

**Table 1. MOF-based electrodes for OER via various optimization strategies**

MOF-based electrodes	$\eta_j = 10$ (mV)	Tafel slope (mV-dec <sup>-1</sup> )	Optimization strategies	Ref.
Ni(Fe)-MOF	227	38.5	Mixed-metal nodes engineering	[78]
NiFe-NPC/NF	240	34	Mixed-metal nodes engineering	[46]
Ni-V MOF	189	76.2	Mixed-metal nodes engineering	[92]
NiRu <sub>0.08</sub> -MOF	187	40	Mixed-metal nodes engineering	[93]
CoZn MOF	287	76.3	Mixed-metal nodes engineering	[94]
MCCF/NiMn-MOFs	280	86	Mixed-metal nodes engineering	[82]
NiFe-btz/NF	239	44.3	Mixed-metal nodes engineering	[81]
FeCoNi-BDC/NF	196	29.5	Mixed-metal nodes engineering	[95]
Ru <sub>0.1</sub> -NiFe-MOF/NFF	197	34.5	Mixed-metal nodes engineering	[96]
FeCoNi-btz/NF	263	64	Mixed-metal nodes engineering	[57]
NiFe-MOF	258 ( $\eta_{100}$ )	34.1	Ligands functionalization	[100]
Ni-DMBD MOF	295	32	Ligands functionalization	[101]
CoBDC-Fc/NF	178	51	Introduction of fragment ligand	[102]
NiFe-MOFs	230	86.6	Lattice strain	[103]
NiFe-NPC	210 ( $\eta_{200}$ )	68	Lattice strain	[104]
$\gamma$ -FeOOH/Ni-MOFNA	193	36	Defect engineering	[118]
FeNiCu-MOFs	269	61	Amorphous engineering	[106]
A-FeNi MOF	152	17	Amorphous engineering	[107]
Ir-Ni-NDC	210	30	Metal-support interfacial bond	[110]
Fe-doped-(NiMOFs)/FeOOH	210	50	Metal-support interfacial bond	[117]
MIL-88A/Ni(OH) <sub>2</sub> -CC	250	46	MOF/LDH heterojunction	[119]
Ni-S/MIL-53(Fe)	256	39	MOF/LDH heterojunction	[120]
MOF-74/LDH	159.7	39.8	MOF/LDH heterojunction	[121]
NiFe-LDH/MOF	208 ( $\eta_{20}$ )	61	MOF/LDH heterojunction	[122]
FeMn-Ni(OH) <sub>2</sub> @MOF/NF	199	26	MOF/LDH heterojunction	[123]

MOF: Metal-organic framework; OER: oxygen evolution reaction; NPC: 1,4-naphthalenedicarboxylic acid; NF: nickel foam; btz: 1,4-bis(4H-1,2,4-triazol-4-yl)benzene; BDC: 1,4-benzenedicarboxylate; NFF: NiFe alloy foam; DMBD: 2,6-dimercaptanbenzene-1,4-dicarboxylate; NDC: 2,6-naphthalenedicarboxylic; MIL: material of Institut Lavoisier; CC: carbon cloth; LDH: layered double hydroxide.

active site to the intermediate and accelerates the reaction kinetics. These are the key parameters for achieving efficient OER electrolysis. Moreover, this strong interfacial electronic effect can elucidate the electronic interactions and charge transfer in MOFs from the valence electron structure point of view based on the test results, such as X-ray photoelectron spectroscopy (XPS) and X-ray absorption near edge structure (XANES). For example, in NiFe MOFs, after the coupling of Ni<sup>2+</sup> and Fe<sup>3+</sup>, the strong repulsion of e<sup>-</sup> between O<sup>2-</sup> and Ni<sup>2+</sup> will induce sectional electron transfer from Ni<sup>2+</sup> to Fe<sup>3+</sup>. In turn, the electronic configuration of the Ni site in the MOF can be well-modulated.

### Bimetallic nodes

Fe-Ni bimetallic compounds are considered to be outstanding OER electrocatalysts to replace noble metal electrocatalysts, such as RuO<sub>2</sub>, IrO<sub>2</sub>, etc., in the past years<sup>[80,90]</sup>. Lin *et al.* prepared a bimetallic MOF electrode including two well-mixed bimetallic MOF phases {Fe-rich FeNi(BDC)[*N,N*-Dimethylformamide (DMF)](F) and Ni-rich FeNi(BDC)(F)} via a one-step solvothermal method [Figure 6A]<sup>[91]</sup>. This electrode contains two well-mixed metal clusters to provide a clear delamination synergy and improve the overall water decomposition efficiency. For Ni-based MOF, introducing other metals with abundant oxidation valence can also greatly improve the catalytic activity of OER. For example, Sun *et al.* prepared a Ni-V MOFs electrode by etching  $\alpha$ -Ni(OH)<sub>2</sub> precursor with terephthalic acid [Figure 6B]<sup>[92]</sup>. V-Ni redox centers of V<sup>+3/+4/+5</sup> and Ni<sup>+3/+2</sup> were successfully introduced into the NiV-MOF electrode, making it a promising oxygen



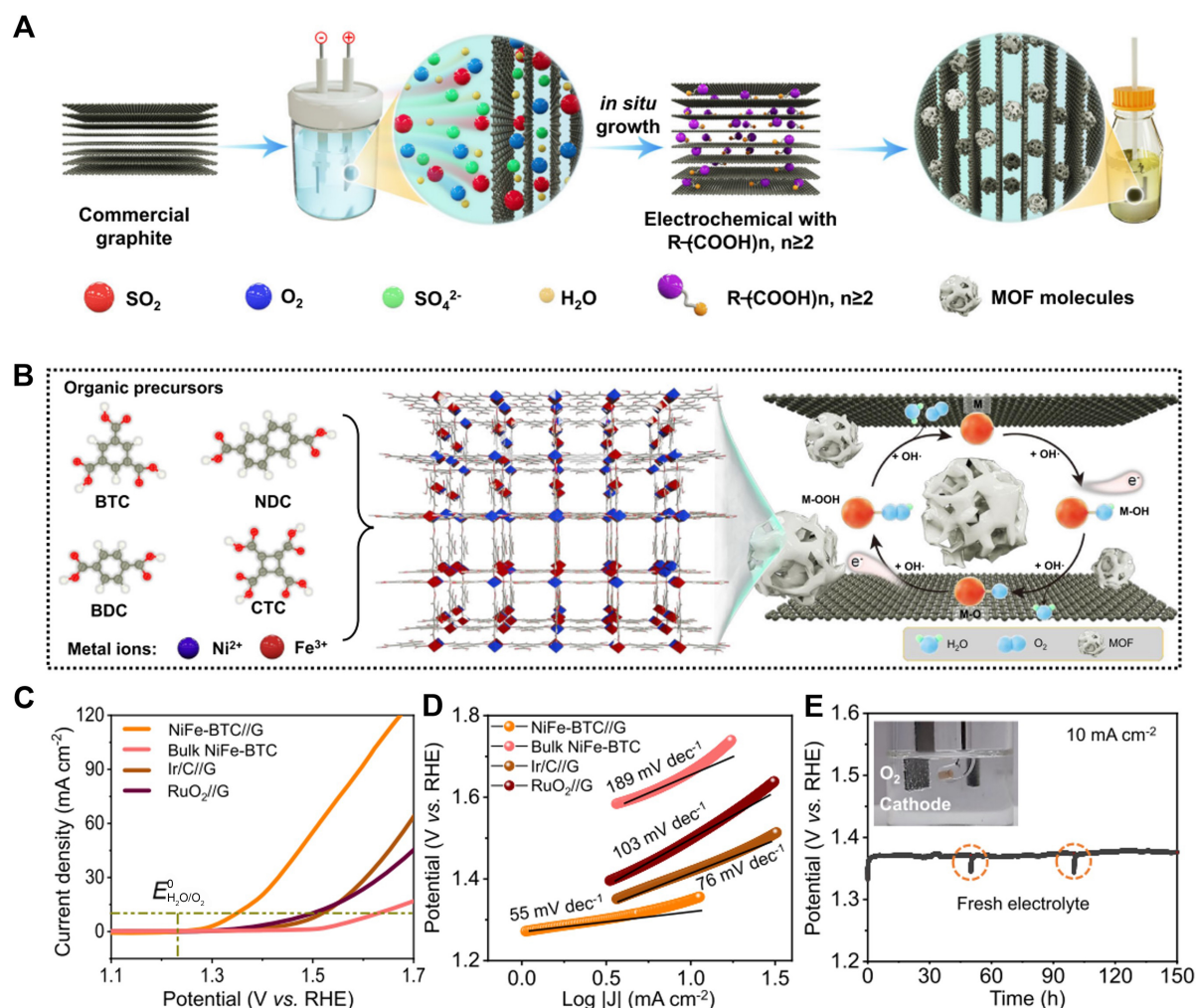


**Figure 5.** (A) Schematic illustration of the electrochemical synthesis process and (B) the resultant NiFe-MOF//G; (C) LSV plots obtained with NiFe-BTC//G, bulk NiFe-BTC, commercial Ir/RuO<sub>2</sub> for OER at  $10 \text{ mV s}^{-1}$  in  $1.0 \text{ M KOH}$  with Ag/AgCl as reference electrode; (D) Tafel plots obtained with NiFe-BTC//G, bulk NiFe-BTC, commercial IrO<sub>2</sub> and RuO<sub>2</sub>; (E) Chronopotentiometric testing of NiFe-BTC//G for 150 h at  $10 \text{ mA cm}^{-2}$  KOH. (A)-(E) were reproduced with permission<sup>[89]</sup>. Copyright 2022, Nature Publishing Group. MOF: Metal-organic framework; LSV: linear sweep voltammetry; BTC: 1,3,5-benzenetricarboxylic acid; OER: oxygen evolution reaction.

electrocatalyst that can reach a current density of  $10 \text{ mA cm}^{-2}$  with an overpotential of 189 mV [Figure 6C and D]. And, at a high current density of  $100 \text{ mA cm}^{-2}$ , the initial activity attenuation of the Ni-V MOF electrode after 100 h is negligible [Figure 6E]. In addition, Li et al. fabricated NiRu<sub>0.08</sub>-MOF electrode with a slightly atomically dispersed Ru as an efficient electrocatalyst. Remarkably, as Ru acts on optimizing the electronic structure of Ni sites, NiRu<sub>0.08</sub>-MOF displayed an overpotential of 187 mV at  $10 \text{ mA cm}^{-2}$  and a Tafel slope of  $40 \text{ mV dec}^{-1}$ . NiRu<sub>0.08</sub>-MOF can also operate continuously for more than 300 h at  $0.1 \text{ M KOH}$ <sup>[93]</sup>. Co-based bimetal MOF is also a promising electrocatalyst for OER. Wu et al. prepared different Co-based MOFs (CoM MOFs/CC, M = Zn, Ni, Cu) *in situ* on CC and systematically compared their structures and OER properties [Figure 6F]<sup>[94]</sup>. At the same time, the effect of the second metal on OER properties of Co-based bimetal MOFs was elucidated. The sequence of OER activity possesses CoZn MOF > CoNi MOF > CoCu MOF > Co MOF according to the results of overpotential and Tafel slope.

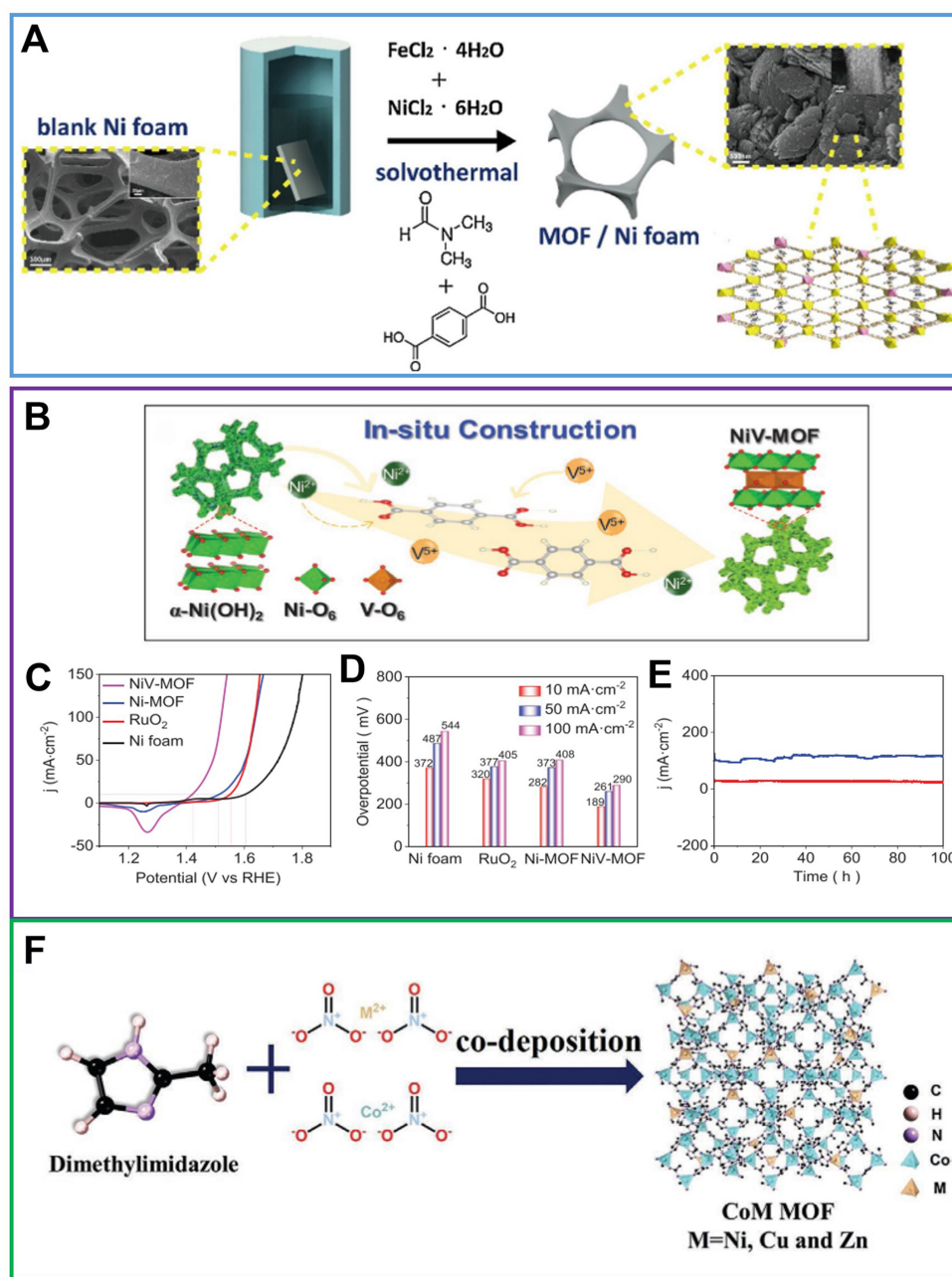


**Figure 6.** (A) Schematic illustration of synthetic process for one-step *in situ* growth of FeNi(BDC)(DMF,F) on NF, reproduced with permission<sup>[91]</sup>. Copyright 2019, Elsevier; (B) Schematic diagram of *in situ* construction of flexible V-Ni redox centers into NiV-MOF NAs; (C) LSV curves of NF,  $\text{RuO}_2$ , Ni-MOF, and NiV-MOF NAs; (D) Comparison of the corresponding overpotentials at current densities of 10, 50, and 100  $\text{mA}\cdot\text{cm}^{-2}$ ; (E) Chronoamperometry test of NiV-MOF NAs measured at 1.46 and 1.52 V vs. RHE for 100 h. (B)-(E) were reproduced with permission<sup>[92]</sup>. Copyright 2021, Wiley-VCH; (F) Synthetic strategy of CoM MOFs/CC, reproduced with permission<sup>[94]</sup>. Copyright 2021, Wiley-VCH. BDC: 1,4-benzenedicarboxylate; DMF: N,N-dimethylformamide; NF: nickel foam; MOF: metal-organic framework; NAs: nanoarrays; LSV: linear sweep voltammetry; RHE: reversible hydrogen electrode; CC: carbon cloth.

### Trimetallic nodes

In addition to bimetallic MOF-based electrodes, trimetallic MOF-based electrodes have recently been reported due to high activity OER electrocatalysis. Li *et al.* prepared a series of Fe/Ni-based trimetallic MOFs [Fe/Ni/Co(Mn)-MIL-53] anchored on NF using solvothermal synthesis that can be directly used as



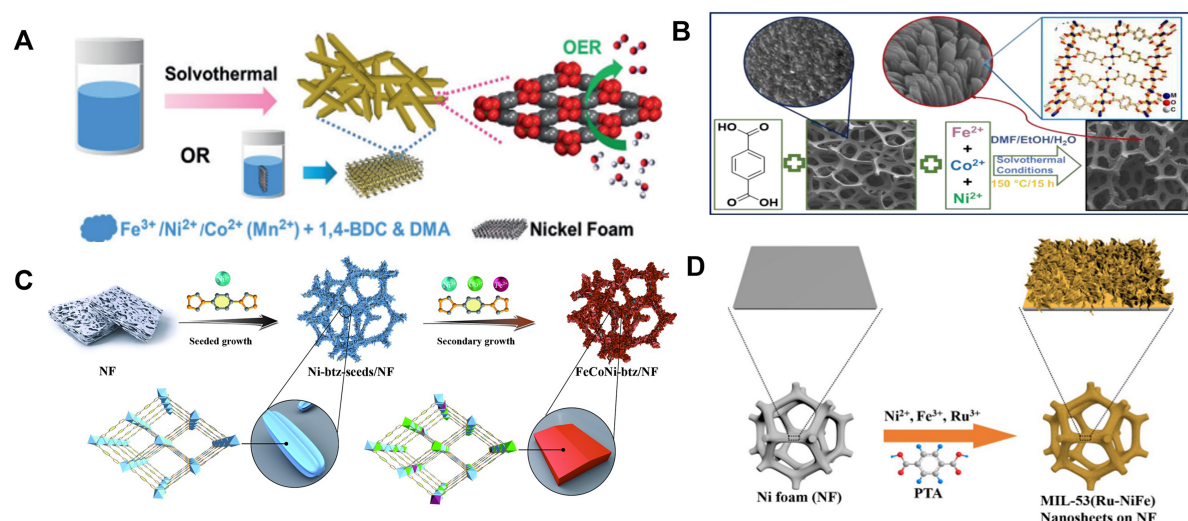


**Figure 7.** (A) Schematic illustration of the preparation of Fe/Ni/Co(Mn)MIL-53 and Fe/Ni/Co(Mn)-MIL-53/NF, reproduced with permission<sup>[40]</sup>. Copyright 2018, Wiley-VCH; (B) Schematic illustration of one-step *in situ* growth of Fe, Co, Ni-based trimetallic MOF thin nanoslabs on NF, reproduced with permission<sup>[95]</sup>. Copyright 2020, Elsevier; (C) Schematic illustration of preparation of FeCoNi-btz/NF electrode, reproduced with permission<sup>[54]</sup>. Copyright 2023, Wiley-VCH; (D) Schematic of synthesis of MIL-53(Ru-NiFe)@NF, reproduced with permission<sup>[97]</sup>. Copyright 2020, Wiley-VCH. MIL: Material of Institut Lavoisier; NF: nickel foam; MOF: metal-organic framework; btz: 1,4-bis(4H-1,2,4-triazol-4-yl)benzene.

OER high-efficiency electrocatalysts [Figure 7A]<sup>[40]</sup>. Similarly, a balanced trimetallic MOF based on Fe, Co and Ni has been developed in order to maximize the electrocatalytic efficiency of multi-component catalysts. Senthil Raja *et al.* prepared Fe-, Co-, and Ni-based trimetallic MOF electrodes which demonstrated excellent OER performance in alkaline aqueous medium, reaching ultra-low overpotentials of 196 and 284 mV at current densities of 10 and 1,000 mA·cm<sup>-2</sup>, respectively<sup>[95]</sup> [Figure 7B]. Additionally, to further increase the adhesion between MOF and NF substrate, our group successfully prepared Fe-, Co-, and Ni-based trimetallic MOF film electrodes using a “twin Ni source” secondary growth method [Figure 7C]<sup>[54]</sup>. It is worth noting that Ru doping strategy greatly improves the OER electrocatalytic activity of NiFe bimetallic MOF<sup>[96]</sup>. For example, Zhao *et al.* grew a Ru-doped Ni/Fe nanosheet [MIL-53(Ru-NiFe)@NF] on NF which showed brilliant OER activity and required only 210 mV to deliver a current density of 50 mA·cm<sup>-2</sup> [Figure 7D]<sup>[97]</sup>. In addition, rare earths, such as Ce, Pr, and Y, are unique four-electron elements that provide a higher catalytic efficiency when combined with active sites such as 3D transition metals<sup>[98]</sup>. This is due to the optimization of Gibbs free energy change ( $\Delta G^\circ$ ) and conductivity via electronic structure adjustment. In detail, Li *et al.* fabricated Y and Ce-doped MOF self-supported electrodes, which can enhance OER performance by constructing rich active sites and multi-metallic synergy<sup>[99]</sup>.

Although various MOF electrodes with mixed-metal nodes have been successfully prepared, it is still difficult to precisely control the content of different metals and their uniform distribution and preserve the morphology and crystallinity of single-metal MOF electrodes. In addition, the introduction of high-valence metals such as W, Mo and other atoms is still worth exploring to obtain superb activity and stability electrodes.

## Ligands design

### *Ligands functionalization*

The organic ligands are another key factor for the coordination structure of MOFs except for metal nodes. Various functional groups (such as  $-\text{NH}_2$ ,  $-\text{SH}$ , *etc.*) can be introduced into the organic ligands to refine the electronic structure of active sites and surface hydrophobicity by post-synthesis or *in situ* methods during preparation of electrodes. Yao *et al.* developed a convenient method to synthesize nitridation-induced NiFe-MOF nanosheets by post-synthetic functionalized terminal ligands [Figure 8A]<sup>[100]</sup>. In detail, NiFe layered LDH (NiFe-LDH) was first grown on the NF surface by hydrothermal deposition, subsequently converted to NiFe-MOF by self-sacrificial template, and finally partial nitridation at 280 °C under  $\text{NH}_3$  atmosphere. The presence of amino ligands can markedly enhance the OER property of NiFe-MOF, requiring only an overpotential of 258 mV at a current density of  $100 \text{ mA}\cdot\text{cm}^{-2}$  with the Tafel slope of  $34.1 \text{ mV}\cdot\text{dec}^{-1}$  in 1 M KOH solution [Figure 8B and C]. As shown in Figure 8D, there is a maximum energy barrier of 1.42 eV of NiFe(NO)-MOF lower than that of NiFe(OOH)-MOF (1.86 eV). When the oxidized NO ligand was introduced into NiFe-MOF, the energy barrier for the conversion from  $\cdot\text{O}$  to  $\cdot\text{OOH}$  was obviously decreased. Density functional theory (DFT) calculations and experimental results showed that  $\Delta G_{\cdot\text{O}}$  optimization can be generated because of irreversible phase remodeling generated by the oxidation of amino ligands before OER, greatly improving OER performance.

In addition, Liu *et al.* designed an adjustable Ni-MOF OER electrocatalyst constructed by a thiol-functionalized 2,6-dimercaptanbenzene-1,4-dicarboxylate (DMBD) ligand<sup>[101]</sup>. As displayed in Figure 9A, a strong chelating motif for  $\text{Ni}^{2+}$  was constituted between the sulfhydryl group and adjacent carboxyl group in DMBD. The distance of lattice fringes in accordance with the *d*-spacing of (001) reflection of crystal structure displayed in the high-resolution transmission electron microscopy (HRTEM) images [Figure 9B]. DFT analysis revealed a metallic electronic structure in Ni-DMBD MOF, indicating that the Ni-S integration function enhances electrical conductivity [Figure 9C]. Moreover, the Ni-DMBD/NF exhibited an overpotential of 295 mV and a Tafel slope of  $32 \text{ mV}\cdot\text{dec}^{-1}$  lower than that of Ni-BDC/NF (337 mV and  $36 \text{ mV}\cdot\text{dec}^{-1}$ ) in the presence of a current density of  $10 \text{ mA}\cdot\text{cm}^{-2}$  [Figure 9D and E]. Additionally, after introducing Fe, the obtained 2D NiFe-DMBD/NF exhibited a lower overpotential of 280 mV for  $\eta_{100}$  [Figure 9F].

### *Introduction of fragment ligand*

Benefiting from the designability of MOF structure, partial replacement of multi-coordinated bridging ligands can be controlled to introduce non-bridging ligands into MOFs without loss of material crystallinity and porosity, accompanied by adjusting their coordination environment and improving catalytic performance. For example, Xue *et al.* developed a fragment ligand introduction strategy to design MOF electrodes for excellent OER performance<sup>[102]</sup>. In detail,  $\text{H}_2\text{BDC}$  and appropriate amount of carboxyferrocene (Fc) reacted with  $\text{Co}(\text{NO}_3)_2\cdot 6\text{H}_2\text{O}$  on NF substrate to construct defective MOF arrays electrodes [Figure 10A and B]. DFT calculations confirmed that  $\text{H}_2\text{BDC}$  in CoBDC can be replaced by Fc to form a novel MOF denoted as CoBDC-Fc. After introducing fragment ligands, the partial density of states (PDOS) of CoBDC-Fc revealed that the generated electronic states near the Fermi level can derived from the changed electronic structure of Co and O. And, this altered band gap and charge distribution can optimize the adsorption intensity of reaction intermediates [Figure 10C-E]. The MOF on NF by direct growth can promote transport kinetics and electrical contact; thus, CoBDC-Fc/NF exhibited brilliant OER activity as the overpotential of 178 mV at  $\eta_{10}$  and Tafel slope of  $51 \text{ mV}\cdot\text{dec}^{-1}$  [Figure 10F-H]. This research develops a fire-new prospect for the evolution of efficient MOF electrodes by introducing fragment ligands.

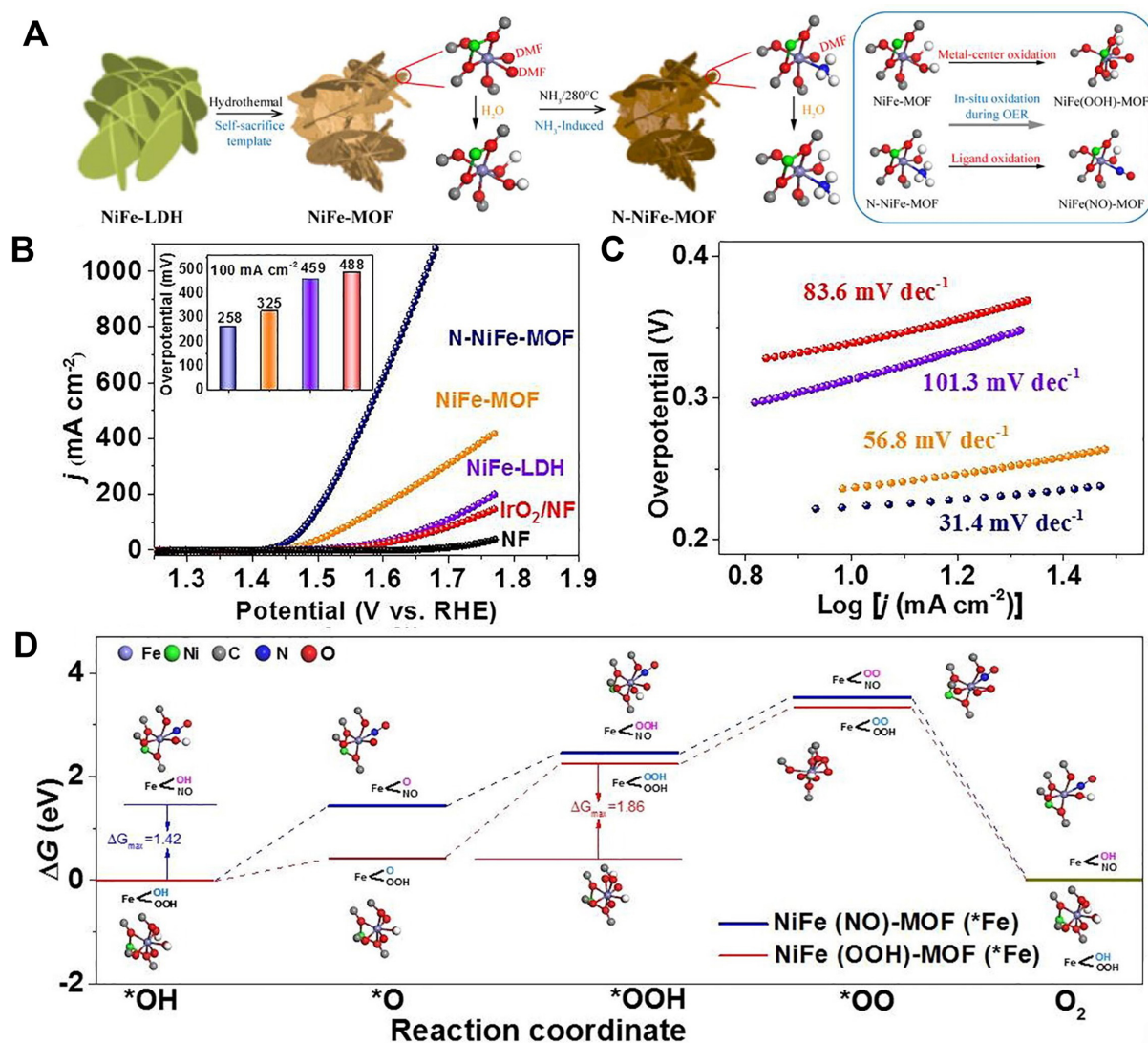


**Figure 8.** (A) Schematic illustration of synthetic process of N-NiFe-MOF; (B) LSV curves of N-NiFe-MOF, NiFe-MOF, NiFe-LDH and IrO<sub>2</sub> with a scan rate of 1 mV·s<sup>-1</sup> (inset: corresponding overpotential at 100 mA·cm<sup>-2</sup>); (C) The corresponding Tafel slope plots from LSV curves; (D) Gibbs free energy illustration by N-NiFe-MOF (\*Fe) and NiFe-MOF (\*Fe) in OER process. (A)-(D) were reproduced with permission<sup>[100]</sup>. Copyright 2022, Elsevier. MOF: Metal-organic framework; LSV: linear sweep voltammetry; LDH: layered double hydroxide; OER: oxygen evolution reaction.

Introducing fragment ligands can induce lattice strain in MOFs via partially replaced multicoordinating ligands. A rational ligand scission method was employed by Ji *et al.* to induce lattice strain in 6% lattice expansion of NiFe-MOFs through the room temperature hydrothermal reactions<sup>[103]</sup>. The lattice strain-induced NiFe-MOFs exhibited efficient OER performance and sustained catalytic stability under alkaline conditions due to changed electronic structures of Ni and Fe. Different from the introduction of fragment ligands above, the direct removal of ligands can also produce lattice strain for MOFs. Cheng *et al.* prepared a NiFe MOF nanosheet array, of which 2,6-naphthalenedicarboxylate acid as the ligand, supported on NF utilizing a low-temperature hydrothermal method, and the thickness of a single nanosheet was ~20 nm<sup>[104]</sup>. Interestingly, as shown in the HRTEM images and powder X-ray diffraction (PXRD) patterns, the interlayer space of lattice-strained NiFe MOF increased by 11.8, 12.0 and 12.1 Å compared to the pristine NiFe-MOF (11.6 Å) after different times of ultraviolet (UV)-treatment [Figure 11A and B]. This is due to the selective



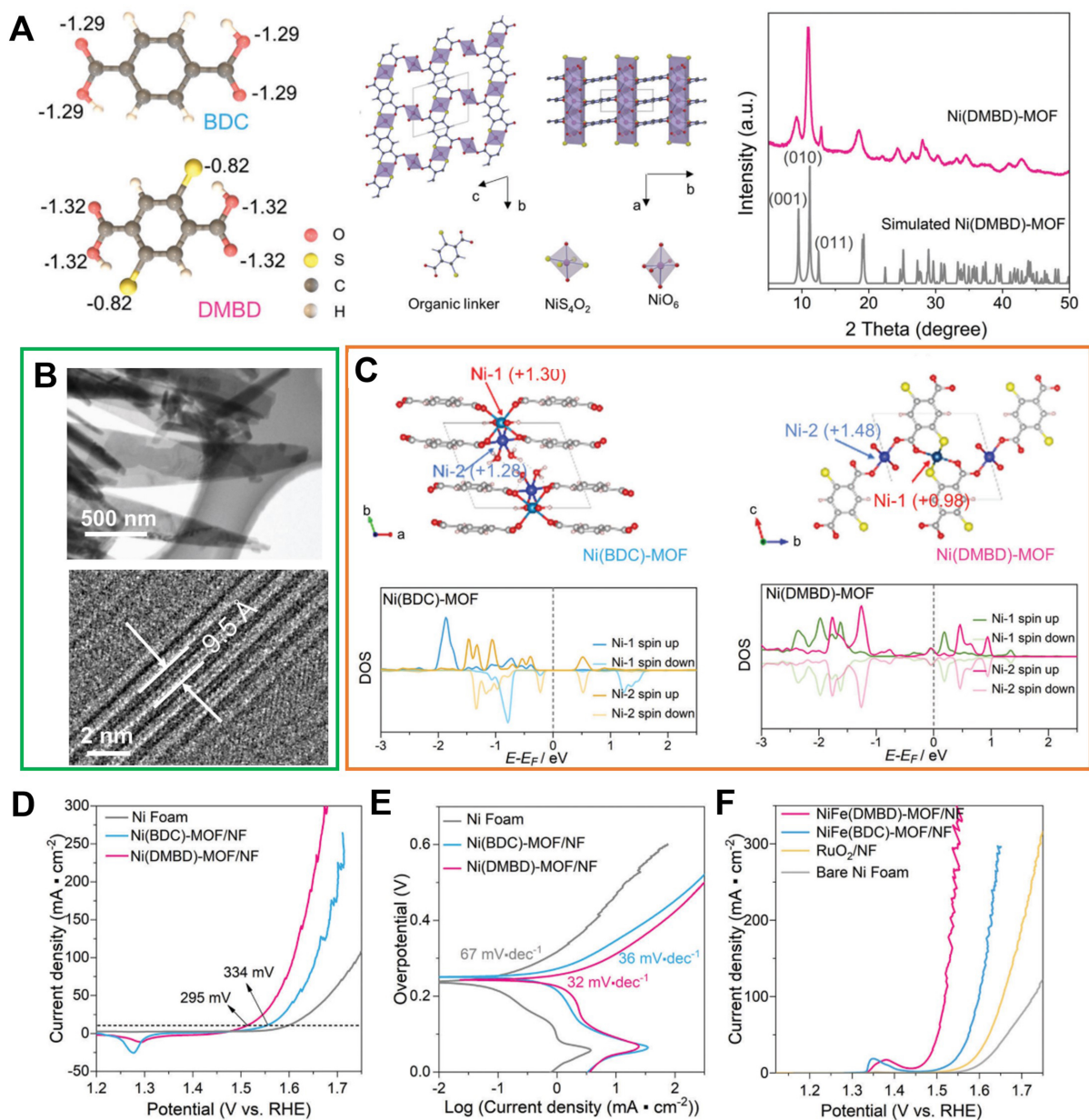


**Figure 9.** (A) Bader charge analysis of deprotonated BDC and DMBD ligands, the identified crystal structure model of Ni(DMBD) and XRD patterns for Ni(DMBD)-MOF from experimental result and simulated one; (B) TEM and HRTEM images presenting the side view of Ni(DMBD)-MOF nanosheet; (C) Scheme of Ni(BDC)MOF and Ni(DMBD)-MOF crystal structure showing the Ni-1 and Ni-2 sites as well as calculated DOS of Ni in Ni(BDC)-MOF and Ni(DMBD)-MOF; (D) OER polarization curves of Ni(BDC)-MOF/NF, Ni(DMBD)-MOF/NF, and bare NF electrode; (E) Tafel plots obtained with Ni(DMBD)-MOF/NF, Ni(BDC)-MOF/NF, and bare NF; (F) LSV plots obtained with NiFe(DMBD)-MOF/NF, NiFe(BDC)-MOF/NF, bare NF, and RuO<sub>2</sub>/NF for OER at 1 mV·s<sup>-1</sup> in O<sub>2</sub> saturated 1 M KOH. (A)-(F) were reproduced with permission<sup>[101]</sup>. Copyright 2022, Wiley-VCH. BDC: 1,4-benzenedicarboxylate; DMBD: 2,6-dimercaptanbenzene-1,4-dicarboxylate; XRD: X-ray diffraction; MOF: metal-organic framework; TEM: transmission electron microscopy; HRTEM: high-resolution transmission electron microscopy; DOS: density of states; OER: oxygen evolution reaction; NF: nickel foam; LSV: linear sweep voltammetry.

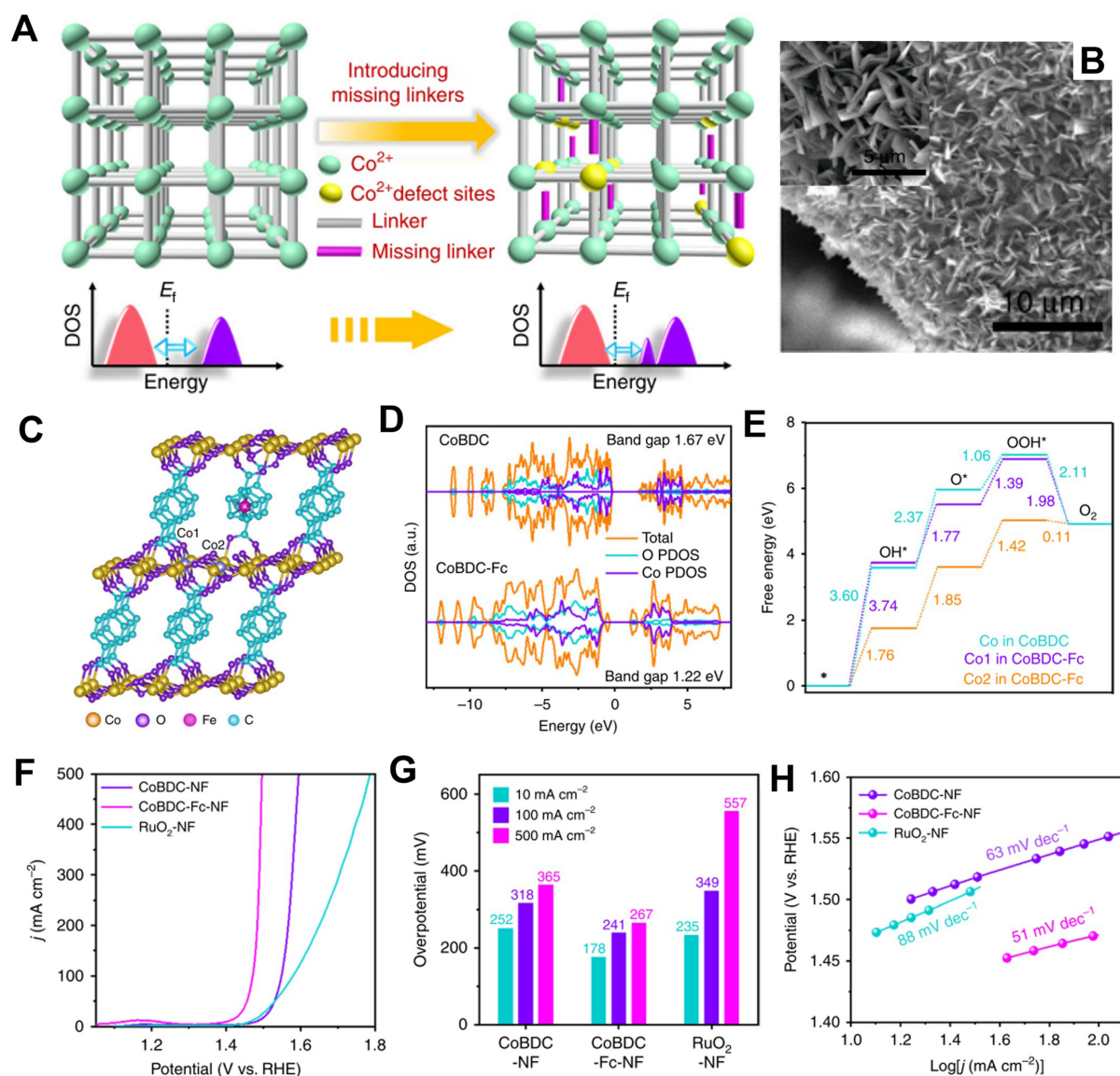


**Figure 10.** (A) Modulating electronic structure of MOFs via introducing missing linkers for efficient OER; (B) TEM image of CoBDC-NF; (C) Crystal structure of CoBDC-Fc obtained from DFT simulation; (D) Calculated DOS of CoBDC and CoBDC-Fc; (E) Free energy diagram for OER on CoBDC and CoBDC-Fc; (F) LSV curves toward OER; (G) Overpotentials at different current densities; (H) Tafel plots of different catalysts. (A)-(H) were reproduced with permission<sup>[102]</sup>. Copyright 2019, Nature Publishing Group. MOF: Metal-organic framework; OER: oxygen evolution reaction; TEM: transmission electron microscopy; BDC: 1,4-benzenedicarboxylate; NF: nickel foam; DFT: density functional theory; DOS: density of states; LSV: linear sweep voltammetry.

dissociation of inactive and unstable  $\pi$ -conjugated naphthyl acid molecules between two metal oxide layers under the action of UV light, which weakens the interaction between the metal oxide layer and organic layer along [100] orientation and contributes to the increase of spacing between metal oxide layers [Figure 11C]. The 4.3%-MOF displayed ultra-low overpotential and a Tafel slope at 200  $\text{mA cm}^{-2}$  than the original MOF and commercial  $\text{RuO}_2$  [Figure 11D]. When the overpotentials were 300 and 400 mV, the mass activities reached up to 2,000 and 3,100  $\text{A g}_{\text{metal}}^{-1}$ , respectively, two orders of magnitude higher than those of pure NiFe MOF and commercial  $\text{RuO}_2$  [Figure 11E]. After continuous OER for 200 h, 4.3%-MOF showed excellent stability, and the initial current density retention rate reached 97% [Figure 11F].

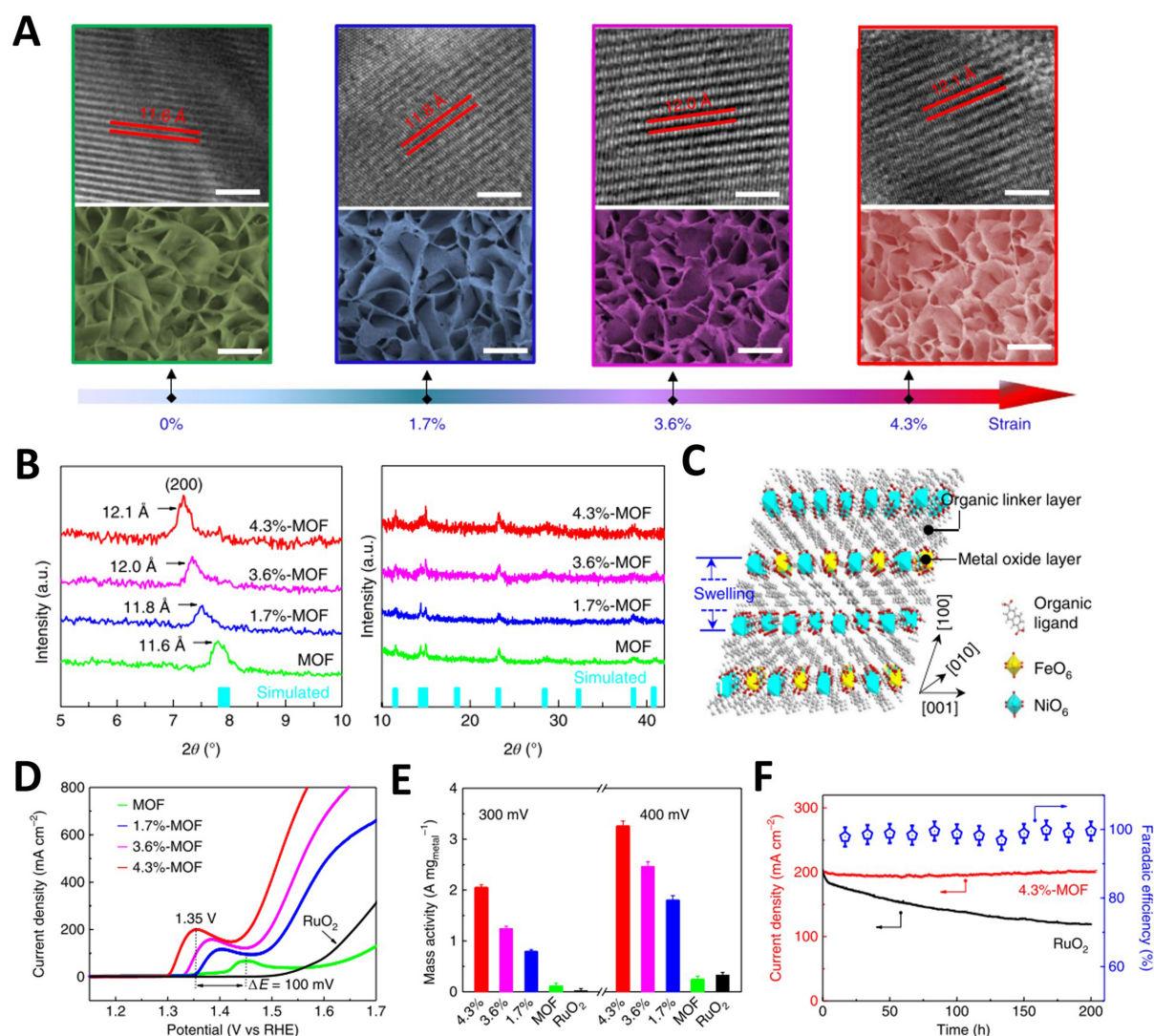


**Figure 11.** (A) HRTEM (top) and SEM (bottom) images of the pristine, 1.7%, 3.6% and 4.3%-MOFs. Scale bars, 5 nm for HRTEM and 200 nm for SEM; (B) XRD patterns for the pristine, 1.7%, 3.6% and 4.3%-MOFs in  $2\theta$  ranges of  $5^\circ$ - $10^\circ$  and  $10^\circ$ - $42^\circ$ , and XRD simulation of the NiFe MOF (turquoise bars); (C) Schematic diagram of crystal structure variation of NiFe MOFs under ultraviolet irradiation. LSV curves (D) and mass activity (E) of OER for the pristine, 1.7%, 3.6% and 4.3%-MOFs and commercial  $\text{RuO}_2$  measured in 0.1 M  $\text{N}_2$ -saturated KOH; (F) OER stability for  $\text{RuO}_2$  and the 4.3%-MOF and OER FE of 4.3%-MOF. (A)-(F) were reproduced with permission<sup>[104]</sup>. Copyright 2019, Nature Publishing Group. HRTEM: High-resolution transmission electron microscopy; SEM: scanning electron microscope; MOF: metal-organic framework; XRD: X-ray diffraction; LSV: linear sweep voltammetry; OER: oxygen evolution reaction; FE: Faradaic efficiency.

## Amorphous engineering

Amorphous MOFs represent a promising family of porous materials that have gained great attention as OER catalysts. Compared to their crystalline counterparts, amorphous engineering of MOFs can increase conductivity and create more defect sites by generating abundant “dangling bonds” and better corrosion resistance<sup>[105,106]</sup>. The structure inheritance in amorphous MOFs is important for maintaining catalytic sites. Meanwhile, the electronic structure can be altered by the presence of a second metal, thus effectively controlling the crucial intermediates about adsorption behavior, thereby expediting reaction kinetics. Li et al. proposed a scalable and facile *in situ* strategy for synthesizing amorphous catalysts derived from MOFs to achieve efficient OER [Figure 12A]<sup>[107]</sup>. They prepared FeNi-MOF under mild conditions and achieved stable MOF loading on a NF substrate. Subsequently, the FeNi-MOF precursor electrode was immersed in



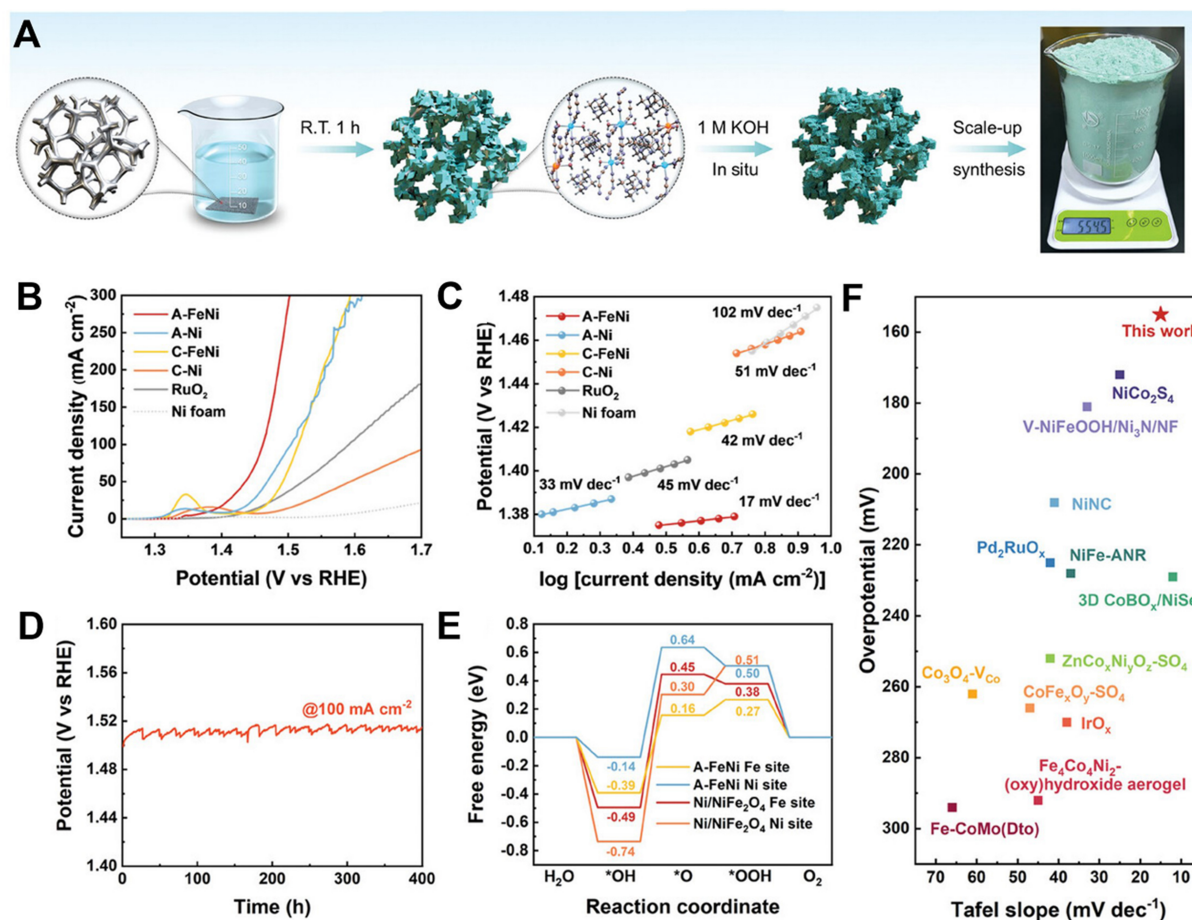


**Figure 12.** (A) The schematic illustration for preparing FeNi-MOF and A-FeNi with a photograph of A-FeNi for scale-up synthesis; (B) LSV curves towards OER; (C) Tafel slope; (D) Durability test for A-FeNi at 100 mA·cm<sup>-2</sup>; (E) Gibbs free energy diagram for A-FeNi at Ni and Fe sites, respectively; (F) Comparison of the OER electrocatalytic properties of A-FeNi to other amorphous catalysts. (A)-(F) were reproduced with permission<sup>[107]</sup>. Copyright 2021, Wiley-VCH. MOF: Metal-organic framework; LSV: linear sweep voltammetry; OER: oxygen evolution reaction.

1 M KOH electrolyte, forming a disordered FeNi-MOF electrode (A-FeNi) with electrocatalytic activity just before the OER process began. It requires low overpotentials of 152 (10 mA·cm<sup>-2</sup>) and 232 mV (100 mA·cm<sup>-2</sup>), respectively, with a Tafel slope of 17 mV·dec<sup>-1</sup> in 1 M KOH [Figure 12B and C]. Notably, A-FeNi exhibits high recyclability and corrosion resistance and can work continuously at 100 mA·cm<sup>-2</sup> for at least 400 h [Figure 12D]. Based on the DFT calculations [Figure 12E], the nickel active site in disordered MOF is crucial in reducing the adsorption energy during the initial step of the OER process. In the following steps of the OER procedure, the Fe active site of A-FeNi becomes the major active site, as indicated by the change in Gibbs free energy. This work could potentially open up new possibilities for designing ultra-high activity amorphous electrocatalysts related to MOFs [Figure 12F].

### Heterostructure engineering

Heterojunction catalysts generally show better catalytic activity than single-component catalysts, which have been widely concerned by researchers recently<sup>[108-115]</sup>. In heterojunction catalysts, electrons can be rearranged at the heterostructural interface to change the properties of active sites. The synergistic effect of different active sites is utilized to promote reaction kinetics, which can reduce the reaction barrier and change the linear scaling relationship.

### *Metal-support interfacial bond*

Rational design of a determined metal-support interfacial bond is regarded as a valid strategy to optimize the inherent activity of MOF electrocatalysts but is still a challenge to date<sup>[116]</sup>. Yang *et al.* constructed an efficient MOF-based self-supported electrode by incorporating well-dispersed Ir nanoparticles (NPs) into the Ni-2,6-naphthalenedicarboxylic (NDC)<sup>[110]</sup>. With the support of Ni-NDC nanosheets, the agglomeration of Ir NPs can be prevented. Meanwhile, the formation of Ni-O-Ir interfacial bonds can optimize the adsorption energy of intermediate products and electron transport kinetics, thus enhancing the electrocatalytic performance. Specifically, the as-prepared Ir@Ni-NDC exhibited ultra-low overpotentials of 210 (1.0 M KOH), 219 (0.5 M H<sub>2</sub>SO<sub>4</sub>) and 296 mV (1.0 M PBS) at  $\eta_{10}$  for OER, respectively.

Li *et al.* elaborately prepared self-supported Fe-doped-(NiMOFs)/FeOOH electrocatalyst with abundant Fe-O-Ni-O-Fe interfacial bonds by interfacial FeOOH and Fe doping engineering [Figure 13A]<sup>[117]</sup>. In detail, the self-supported Ni-MOF electrode was first prepared via solvothermal treatment in the presence of NF. The as-prepared Ni-MOF electrode, as an anode, conducted electrodeposition in the solution of Fe<sup>3+</sup>. During the post-modification process, Fe<sup>3+</sup> replaced part of Ni<sup>2+</sup> in Ni-MOFs through ion exchange, and the remaining Fe<sup>3+</sup> ions were spontaneously oxidized into FeOOH nanodots. Fe-O-Ni-O-Fe interfacial bonds were successfully constructed to promote the distorted coordination structure of Ni sites, facilitating redistributed charge density of Ni/Fe and regulating the adsorption energy of intermediates near the optimal *d*-band center. Fe-doped-(NiMOFs)/FeOOH displayed superior catalytic performance for OER with a low  $\eta_{15}$  of 210 mV and low Tafel slope of 50 mV·dec<sup>-1</sup> under alkaline conditions. Similarly, Ni *et al.* developed Ni-MOF nanosheet arrays with linker defects by a simple approach based on UV/ozone treatment, further inducing  $\gamma$ -FeOOH nanosheets to build a rich oxyhydroxide/MOF heterostructure interfaces by growing on the surface of Ni-MOF [Figure 13B]<sup>[118]</sup>. In addition, the apparent compressed lattice strain of MOF nanosheets in  $\gamma$ -FeOOH/Ni-MOFNA samples revealed successful formation of heterostructure interfaces. Through the analysis of X-ray absorption spectroscopy (XAS) measurement, XPS spectroscopy, and so on, the optimized  $\gamma$ -FeOOH/Ni-MOFNA electrode with a low metal coordination number and abundant oxygen vacancy exhibited excellent performance for OER in an alkaline environment.

### *MOF/LDH heterojunction*

Heterojunction materials, such as MOF/LDH, have been considered as one of the most promising OER electrocatalysts in recent years<sup>[119,120]</sup>. However, their application has also been hampered by complex multi-step synthesis processes that introduce cost, complexity and reproducibility issues. To address these problems, Mu *et al.* demonstrated a kinetic controlled synthesis strategy to obtain bimetallic MOF/LDH heterojunction electrodes with a multi-layered structure [Figure 14A]<sup>[121]</sup>. The highly porous NiFeLDH nanosheet network was vertically distributed on the surface of the NiFe-MOF-74 microprism. The above results can increase high exposure of active sites and promote rapid mass transfer, achieving excellent OER catalytic performance. The optimal electrode prepared by Fe<sup>3+</sup> as the only metal ion and 2,5-dihydroxyterephthalic acid (DHTP) as an organic ligand using kinetic control during the solvothermal process. This consists of four stages: (1) fast construction of Fe(III)-MIL-53 nanosheets; (2) construction of bimetallic NiFe-MOF-74 microprisms and dissolution of MIL-53; (3) NiFe-LDH and NiFe-MOF-74 prisms competed for growth and formed a hierarchical heterojunction structure; (4) thermodynamically stabilized NiFe-MOF-74 large single crystals formation over a longer period of time, losing the delamination feature [Figure 14B and C]. As shown in Figure 14D, a thermodynamic metastable intermediate state with hierarchical heterojunction structure was obtained as the LDH nanosheet array grown vertically on the MOF-74 microprism. The MOF/LDH heterostructures were first designed using one-step solvothermal methods. Xiao *et al.* analyzed the adsorption free energy of intermediates for NiFe-LDH/MOF during OER

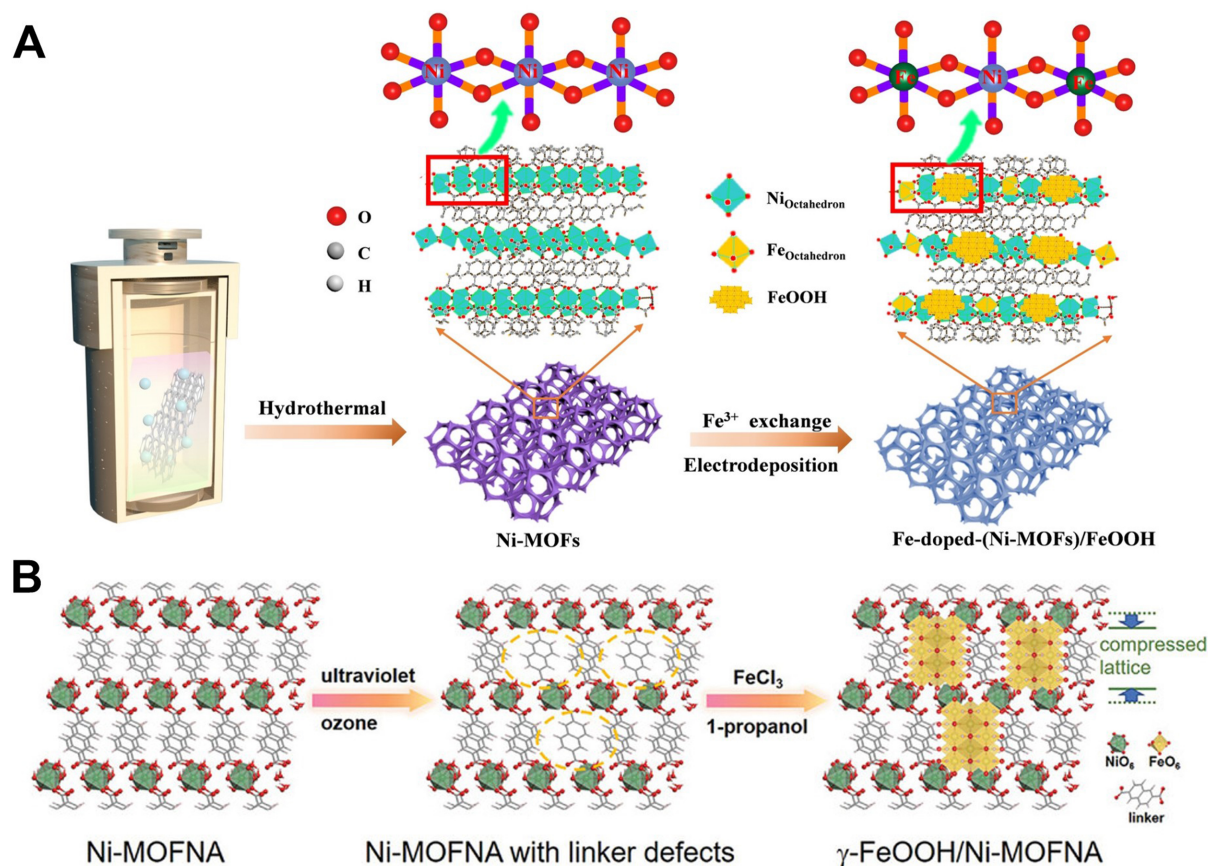


**Figure 13.** (A) Schematic illustration of synthesis process of Fe-doped-(Ni-MOFs)/FeOOH with interfacial Fe, reproduced with permission<sup>[117]</sup>. Copyright 2022, Wiley-VCH; (B) Schematic illustration of fabrication process of  $\gamma$ -FeOOH/Ni-MOFNA, showing the structural change of Ni-MOFNA, reproduced with permission<sup>[118]</sup>. Copyright 2023, Wiley-VCH. MOF: Metal-organic framework.

by DFT calculations to explore the inherent properties of NiFe-LDH/MOF<sup>[122]</sup>. By comparison, Ni sites in heterostructured NiFe-LDH/MOF were the active centers and the rate-determined step at Ni adsorption site changes correspondingly confirming the decrease of the reaction energy barrier generated by the two-phase coupling heterostructure [Figure 14E and F]. Meanwhile, the Gibbs free energy of the oxygen-containing intermediates adsorption also can be optimized in NiFe-LDH/MOF heterostructure, thus accelerating the OER kinetics. They also prepared NiFe-LDH/MOF nanosheet arrays on the NF substrate via a two-step hydrothermal reaction process [Figure 14G]. The results showed that NiFe-LDH/MOF required only 208 and 275 mV OER overpotentials at  $\eta_{20}$  and  $\eta_{100}$ , with a low Tafel slope of 61 mV·dec<sup>-1</sup> [Figure 14H and I].

In addition to growing LDH on MOF to construct heterostructures, LDH can also be grown and employed as a semi-sacrificial template to prepare MOFs on LDH heterostructures. Zheng *et al.* converted FeNi LDH to corresponding FeNi MOF via *in situ* methods, building 2D/1D FeNi LDH-MOF hybrid arrays as a high-performance catalyst for OER [Figure 15A]<sup>[79]</sup>. In detail, at the first, using Fe(NO<sub>3</sub>)<sub>3</sub> and Ni(NO<sub>3</sub>)<sub>2</sub> as metal sources, FeNi-LDH nanosheets were prepared using hydrothermal methods and grown uniformly on the CC surface. Then, DHTP coordinated with FeNi-LDH as a semi-sacrificial template for MOF nanocrystal growth and *in situ* phase reconstruction. Subsequently, 2D/1D FeNi LDH/MOF was formed via 2D FeNi-LDH nanosheets grafted with 1D swordlike FeNi-MOF crystals. Accompanied by an increase of coordination reaction time, 1D swordlike crystals formed. The nanosheets gradually turned thin and eventually became MOF nanocrystals [Figure 15B-E]. Similarly, Ye *et al.* prepared MOF and hydroxide



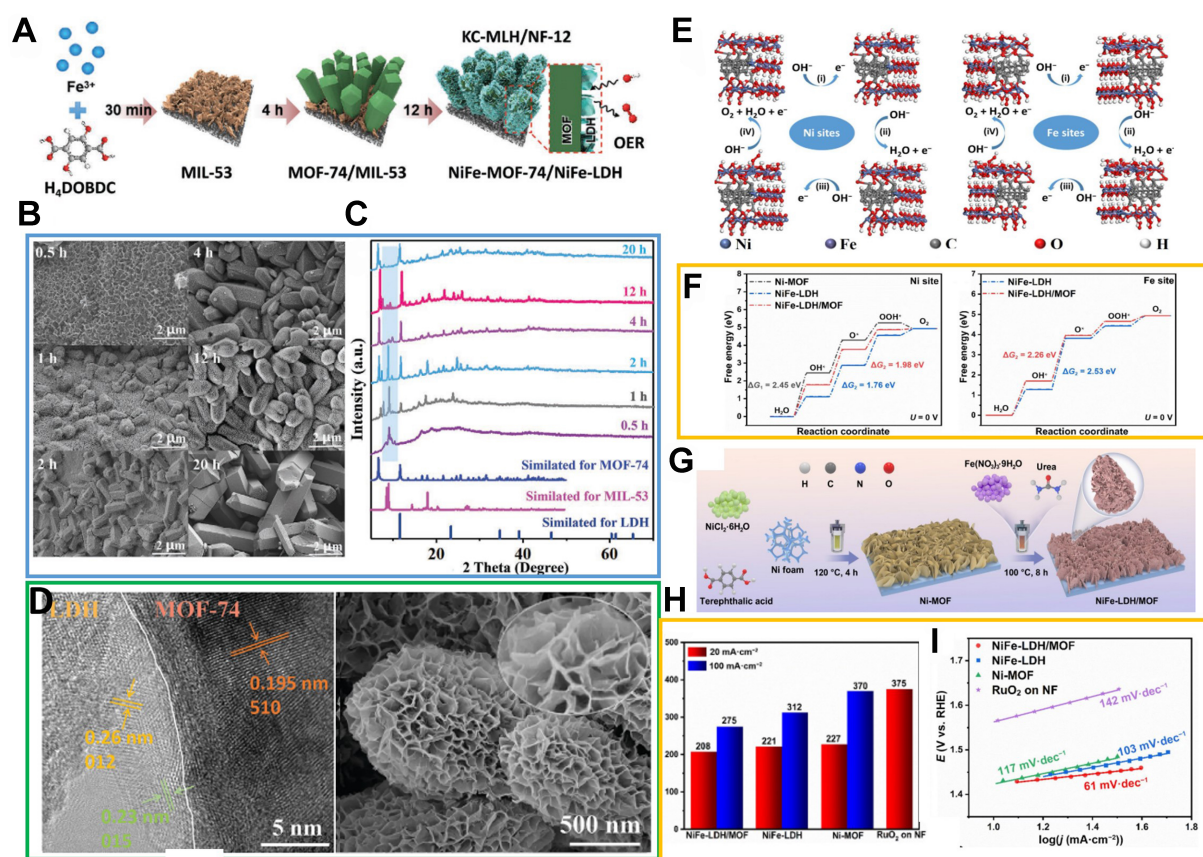


**Figure 14.** (A) Schematic illustration of structural evolution during kinetic-oriented formation of KC-MLH/NF-12 electrodes with different reaction times; (B) SEM images of heterostructures obtained from 0.5, 1, 2, 4, 12, and 20 h reactions; (C) corresponding XRD patterns in comparison with simulated standard references; (D) TEM images of KC-MLH/NF-12 and corresponding HRTEM image. (A)-(D) were reproduced with permission<sup>[121]</sup>. Copyright 2023, Wiley-VCH; (E) Four-electron mechanism of OER on Ni sites and Fe sites in NiFe-LDH/MOF models; (F) Calculated free-energy diagram of OER intermediates at zero potential for different models; (G) Schematic illustration of construction for NiFe-LDH/MOF nanosheet array on NF substrate; (H) Overpotential diagram (@20 and 100 mA·cm<sup>-2</sup>) corresponding to the polarization curves of OER; (I) Tafel slope plots. (E)-(I) were reproduced with permission<sup>[122]</sup>. Copyright 2023, Springer. KC-MLH: Kinetic-controlled MOF-LDH heterojunctions; NF: nickel foam; SEM: scanning electron microscope; XRD: X-ray diffraction; TEM: transmission electron microscopy; HRTEM: high-resolution transmission electron microscopy; OER: oxygen evolution reaction; LDH: layered double hydroxide; MOF: metal-organic framework.

complexes on FeMn-Ni(OH)<sub>2</sub> nanosheets by a ligand etching strategy<sup>[123]</sup>.

To summarize, regardless of the control method, the most fundamental lies in the strong interfacial electronic effect generated, which modulates the electronic structure of the active site, ameliorating the binding energy between intermediates and active sites to facilitate the reaction kinetics. Despite various modulation strategies, the currently reported applications of MOF-based self-supported electrodes under high current density conditions still face major challenges: (1) During the OER process, even at low current densities, due to the strong alkaline environment and the effect of the applied electric field, MOFs usually undergo the reconfiguration of the surface electronic structure or even the overall structural change, resulting in the inability of MOFs to fully utilize the advantages of periodic lattice structure; (2) Compared with the case of low current density, the application at high current density requires not only a larger scale of charge and mass transfer, but also higher intrinsic activity of active sites to enable the reaction to occur rapidly, which also places higher requirements on the electrical conductivity and mass transfer capability of catalyst; (3) At high current density, a large number of H<sub>2</sub> bubbles cover the surface of the self-supported

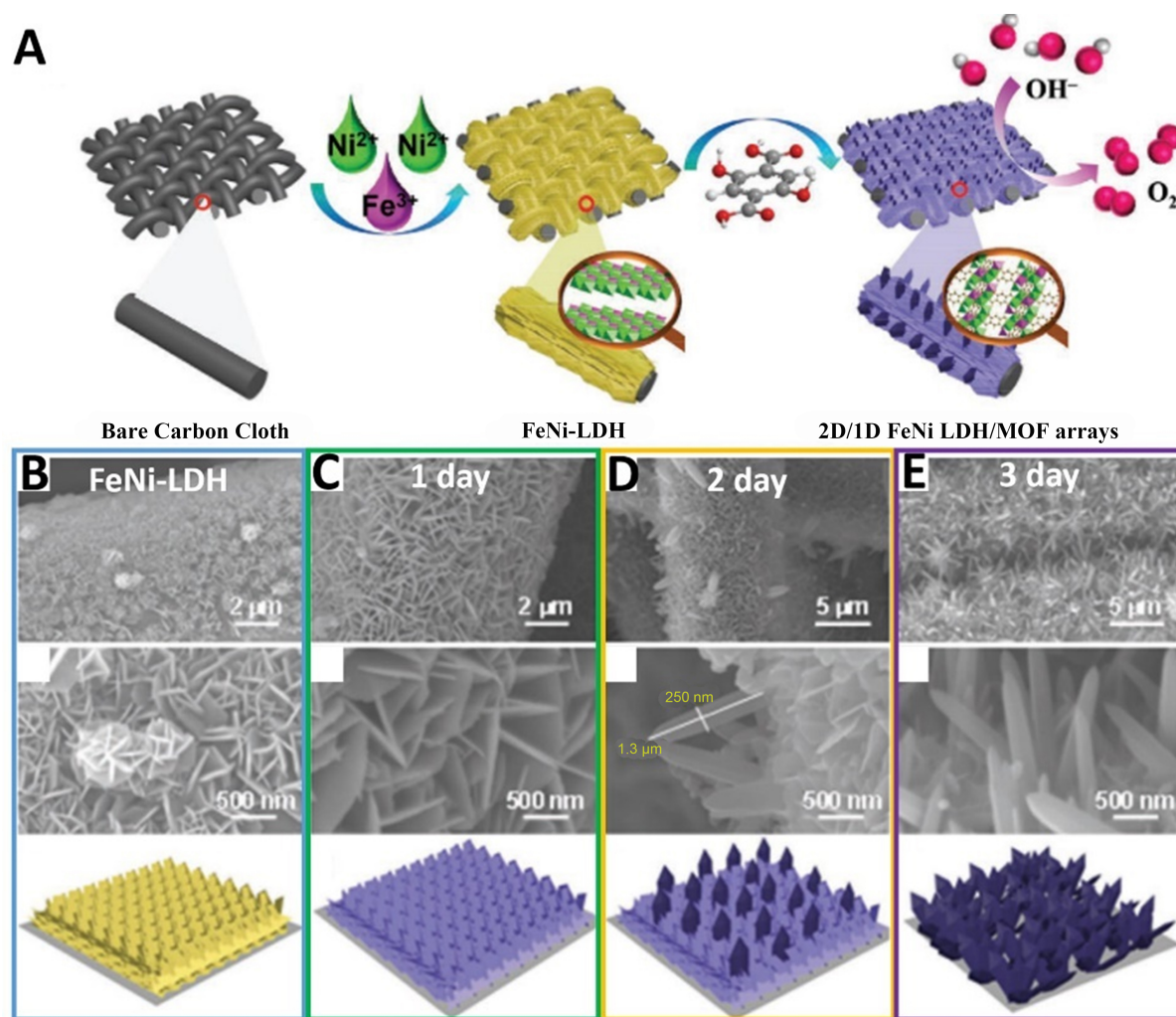


**Figure 15.** (A) Schematic illustration of 2D/1D FeNi LDH/MOF arrays preparation; (B)-(E) SEM images of schematic illustration for morphology evolution of FeNi-LDH during coordination reaction under different conditions. (A)-(E) were reproduced with permission<sup>[79]</sup>. Copyright 2021, Wiley-VCH. LDH: Layered double hydroxide; MOF: metal-organic framework; SEM: scanning electron microscope.

electrode of MOFs, which seriously affects the exposure of the active sites, hinders both charge and mass transfer, and makes it difficult to maintain its long-term OER activity. Therefore, further rational microstructure/component design of self-supported electrodes for MOFs is an effective way to solve these problems.

## OER MECHANISM BY POST ANALYSIS AND OPERANDO CHARACTERIZATION TECHNOLOGIES

MOF-based electrodes show excellent OER stability and catalytic performance through different adjustment strategies. However, the catalytic mechanism research is still a difficult point. Due to the action of electrolytes and the applied electric field during OER, MOF-based electrodes usually undergo surface geometry and electronic structure reconstruction and even the overall structure change. Therefore, a thorough understanding of the *in situ* structure evolution of electrocatalyst under actual conditions, determination of its authentic active site, and the exploration of catalytic mechanism have become the key factors for rational design and optimization of MOF electrodes with ideal catalytic properties<sup>[124-126]</sup>.

In general, the weak coordination bonds between metal nodes and organic linkers are compared to ionic bonds and covalent bonds. Typical electrocatalysis includes chemical and electrochemical environments, such as dynamic electrochemical double-layer interfaces, internal sphere electron transfer and surface redox reactions [Figure 16]<sup>[107]</sup>. Hence, the structural integrity of MOFs under an electrochemical environment is worth exploring, whether as catalyst or pre-catalyst<sup>[127,128]</sup>.

Wang *et al.* developed a kind of stabilized bimetallic FeNi-MOF nanoarray electrodes built with organic linkers of H<sub>2</sub>TDC on NF for electrocatalytic activities in OER [Figure 17A]<sup>[73]</sup>. Interestingly, electrocatalytic performance in MOF electrodes continually increases under CV cycles until reaching a steady state. Systematic post-catalysis investigations were conducted on FeNi-MOFs after different CV cycles to explain the MOF structure. As shown in Figure 17, X-ray diffraction (XRD) patterns of Ni-MOFs and FeNi-MOFs after varying cycles were unchanged compared with the pure one, remaining undamaged during the cycle test. Fourier transform infrared spectroscopy (FTIR) and Raman spectra also confirmed the structure integrity, which showed a constant vibration pattern after the CV cycle test [Figure 17C and D]. According to transmission electron microscopy (TEM) and selective area electron diffraction (SAED) analysis, it can be concluded that the FeNi-MOF electrode has maintained its nanoribbon morphology and single crystal properties with more CV cycles [Figure 17E]. As shown in Figure 17F, the fine OER performance of FeNi-MOF electrodes is attributed to partial transformation of Fe<sup>2+</sup> to Fe<sup>3+</sup> ions. The self-optimized FeNi-MOF electrodes as catalysts exhibited excellent OER activity at stable states with the Tafel slope of 52.4 mV·dec<sup>-1</sup>, a low overpotential of 266 mV at 100 mA·cm<sup>-2</sup>, and ultrahigh structure stability [Figure 17G].

Although a small number of MOF electrodes could maintain structural integrity after OER tests, most MOFs were driven by a strong electric field, which changed their surfaces or overall electronic or geometric structures. Therefore, structural characterizations only after catalysis are not enough; operando characterization techniques combined with electrochemistry are highly required and more accurate to investigate the structural changes of MOFs during OER. Operando characterization techniques can capture the OER intermediates, explore structural changes of catalysts, and understand the effective relationship between structure and OER performance during OER. With operando characterization techniques, samples can be continuously and synchronously analyzed, and the OER process and structural morphological changes are under real-time observation. Operando XAS analysis can verify active sites, oxidation state, bonding types and amounts, and atomic distance deviations during OER. For example, through operando XAS characterization, Cheng *et al.* observed a structural transition from the original Br-Ni-MOF to  $\gamma$ -Ni(OH)<sub>2</sub> analogs and then to  $\gamma$ -NiOOH phases during this process [Figure 18A]<sup>[129]</sup>.

Operando synchrotron-radiation (SR)-FTIR measurements of reactive intermediates during OER were carried out by Sun *et al.* using a self-made rooftop reflector infrared device, and the promotion of OER activity by a flexible V-Ni redox center was demonstrated<sup>[92]</sup>. As shown in Figure 18B, a new absorption peak slowly appeared at 1,170-1,330 cm<sup>-1</sup> as the potential increased from 1.2 to 1.6 V with respect to the reversible hydrogen electrode (RHE). An absorption band appeared at 3,440 cm<sup>-1</sup>, corresponding to the stretching pattern of adsorptive H<sub>2</sub>O molecule. Interestingly, the strength of the absorption band (1,170-1,330 cm<sup>-1</sup> belonging to Fe/Co/Ni-O<sup>+</sup>) significantly increased when the potential rose to 1.4 V and tended to stabilize with further increase in potential, showing the enrichment of reaction intermediates during OER. These results indicated that the authentic OER active site in NiV-MOF nanoarrays (NAs) was Ni rather than V.

Operando Raman spectroscopy is the most used *in situ* characterization technique, which also can elucidate the state and structural evolution of metal on the catalyst surface during OER<sup>[69]</sup>. For example, Liu *et al.*



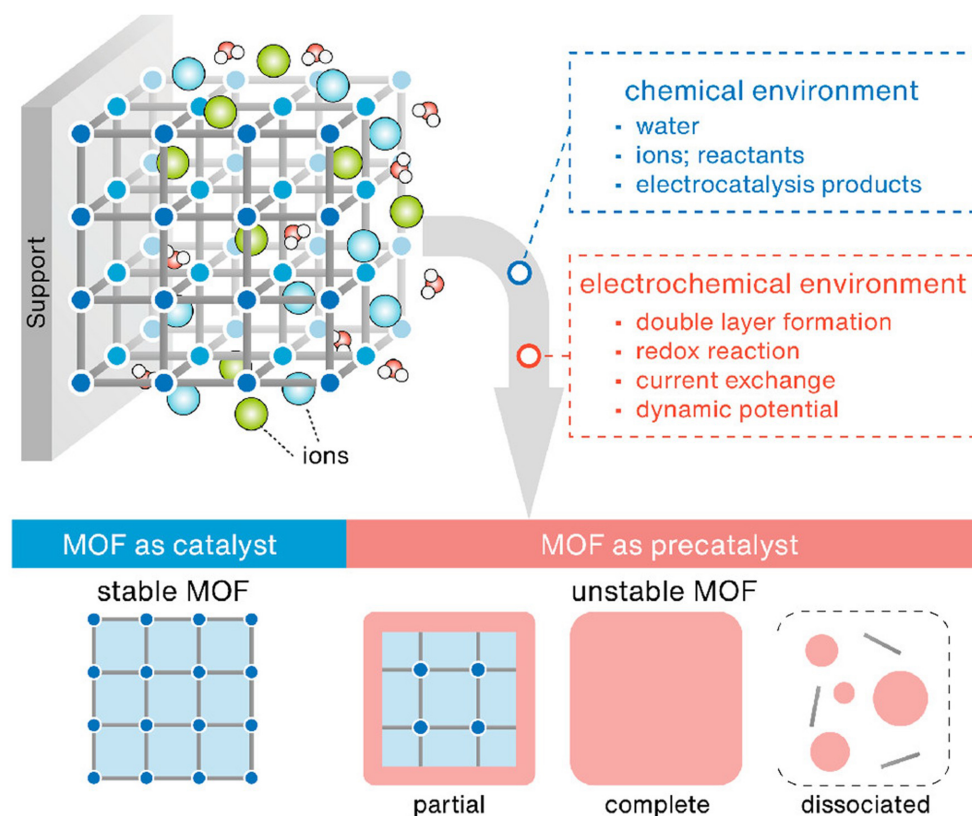


**Figure 16.** Chemical and electrochemical environments of MOFs during electrocatalysis and possible scenarios: stable and unstable (partial and complete conversion, dissociation), reproduced with permission<sup>[126]</sup>. Copyright 2022, American Chemical Society. MOF: Metal-organic framework.

performed operando Raman tests under different voltages to explore the evolution mechanism of MOF active sites during OER<sup>[130]</sup>. At low voltages, FeNi-2,5-dihydroxy-1,4-benzoquinone(DHBQ)/NF peaks were located at 461 and 530  $\text{cm}^{-1}$ , which are defects or disordered in  $\text{Ni}^{2+}$  and  $\text{Fe}^{3+}$  substances, respectively. As the voltage was increased to 1.55 V, a peak at 530  $\text{cm}^{-1}$  reappeared, corresponding to  $\text{NiO}_x$  species, and was more pronounced at 1.60 V. Raman spectroscopy of FeNi DHTP/NF showed a transition from  $\text{Ni}^{2+}$  to  $\text{Ni}^{3+}$  at 1.50 V, producing the key  $\text{NiOOH}$  active substance [Figure 18C]. Similarly, to elucidate precise crystal structure of generated  $\gamma$ - $\text{NiOOH}/\beta$ - $\text{NiOOH}$  by  $\text{NiOOH}$ , Dai *et al.* further collected high-resolution Raman spectra from 300 to 700  $\text{cm}^{-1}$  of Ni-MOF after 100 cyclic CV tests. Notably,  $\beta$ - $\text{NiOOH}$  and  $\gamma$ - $\text{NiOOH}$  phases have similar structures [Figure 18D]<sup>[131]</sup>.

In summary, *in situ* characterization alone is insufficient to fully understand the reaction mechanism of MOF electrodes and identify the active centers, although *in situ* characterization can capture the reaction intermediates online to explore the electronic and geometric structure of the MOF electrode surface. Therefore, it is necessary to use post-catalytic characterization tools (XRD, Raman, HRTEM, BET, XPS, and XANES) to investigate whether the crystal structure, electronic structure, pore structure, and morphology of MOF electrodes change after catalysis. Then, the MOF structure can be accurately simulated using the Vienna ab initio simulation package (VASP) or Material Studio software. The free energies of adsorption of OER reaction intermediates are calculated based on DFT theory to determine the active site and deceleration step, the electronic structure of the active site, the electron transfer between distinct components, and the adsorption capacity of the active site for intermediates.

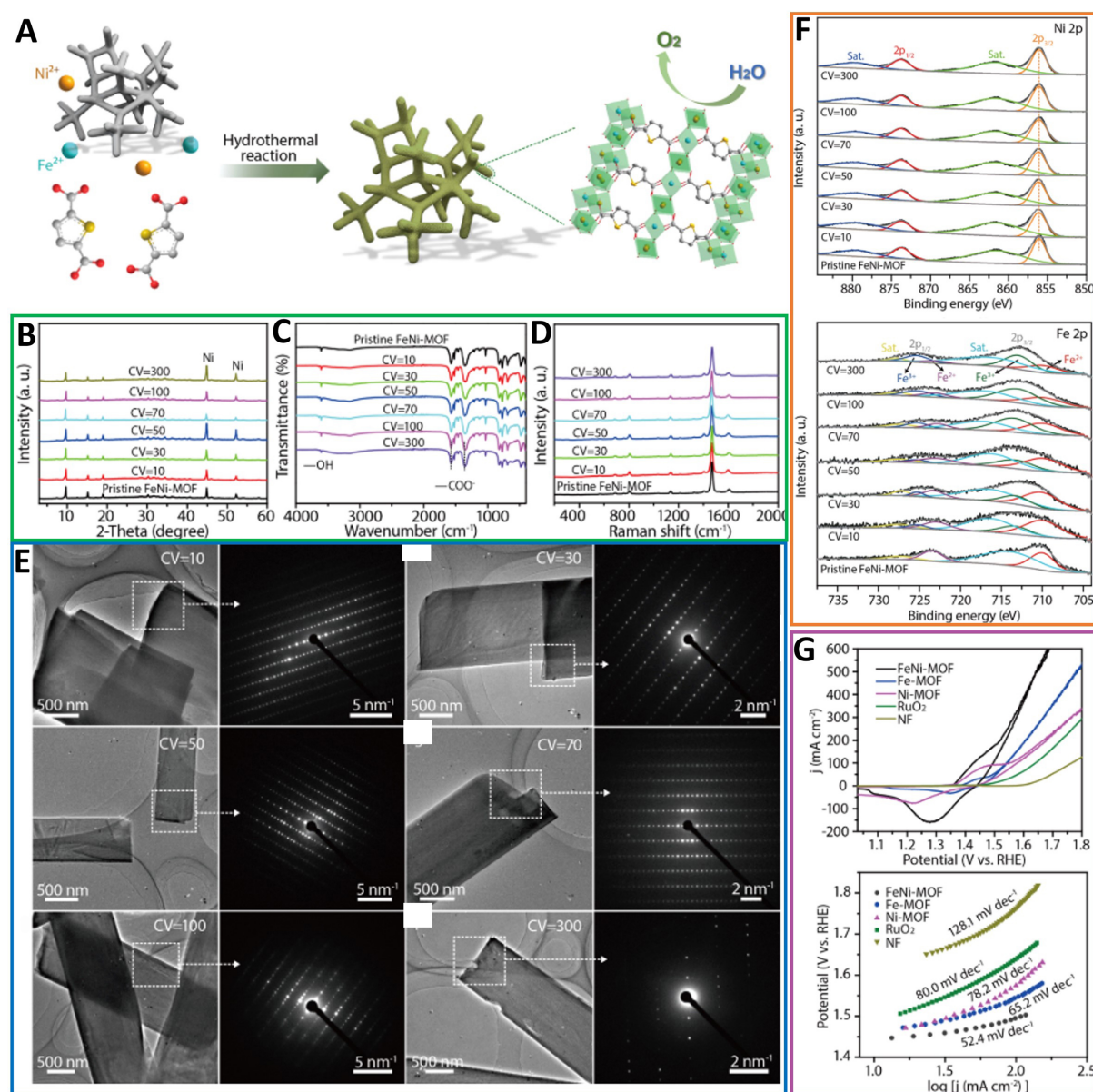


**Figure 17.** (A) Schematic illustration of synthesis of FeNi-MOF nanoarrays via a hydrothermal method. Structural characterizations of FeNi-MOF nanoarrays after various CV cycles; (B) XRD patterns and (C) FTIR and (D) Raman spectra of FeNi-MOF nanoarrays after different CV tests; (E) TEM images and the corresponding SAED patterns for FeNi-MOF nanobelts after different CV cycles; (F) Ni 2p and Fe 2p XPS spectra of FeNi-MOFs after different CV cycles; (G) Electrocatalytic properties of FeNi-MOF nanoarrays and other samples for OER and Tafel plots of different catalysts. CV curves toward OER at a scan rate of  $5 \text{ mV}\cdot\text{s}^{-1}$ . (A)-(G) were reproduced with permission<sup>[73]</sup>. Copyright 2021, American Chemical Society. MOF: Metal-organic framework; CV: cyclic voltammetry; XRD: X-ray diffraction; FTIR: Fourier transform infrared spectroscopy; TEM: transmission electron microscopy; SAED: selective area electron diffraction; XPS: X-ray photoelectron spectroscopy; OER: oxygen evolution reaction.

## OER MECHANISM STUDY BY DFT CALCULATIONS

DFT was utilized to gain insight into the OER catalytic performance improvement by calculating Gibbs free energy of OER intermediates, Bader charges, density of states, and energy bands. Most MOF-derived electrodes follow the four-electron AEM to evaluate their intrinsic activity in OER under alkaline conditions. Zhao *et al.* explored the promoted mechanism of OER performance for  $\text{Ni}_{0.5}\text{Fe}_{0.5}$ -tetrahydroxy-1,4-benzoquinone hydrate (THQ)<sup>[132]</sup> using AEM. First, catalyst structures for DFT theoretical calculations

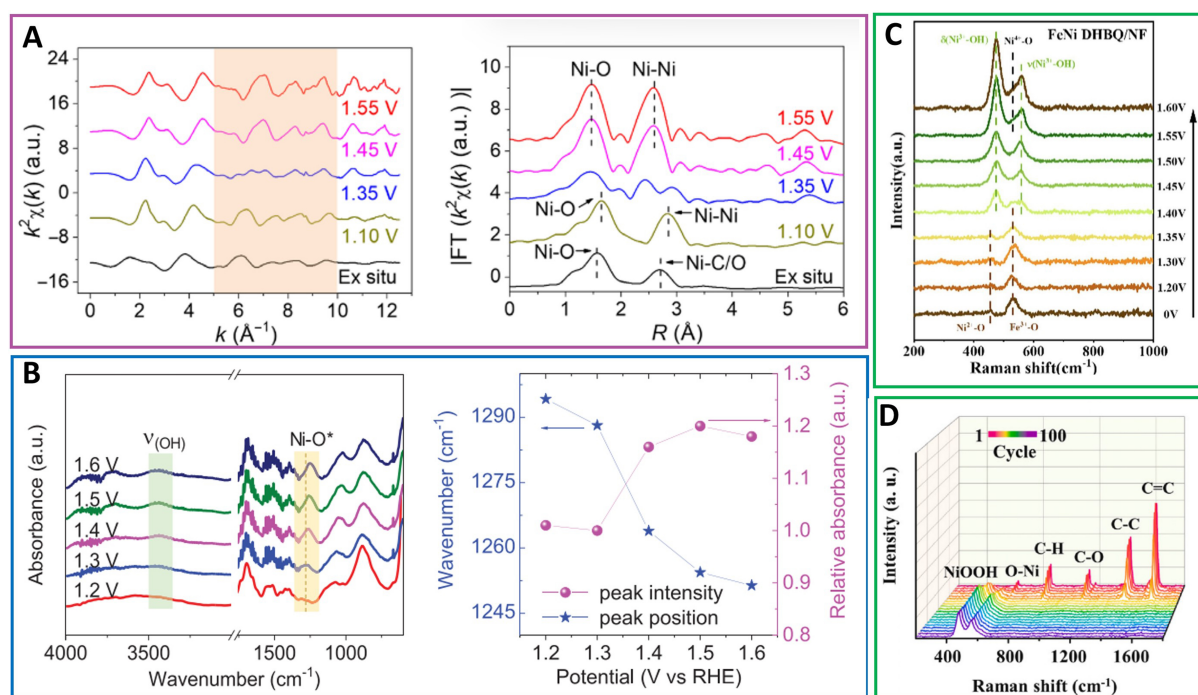


**Figure 18.** (A) The  $k^2\chi(k)$  oscillation curves and Fourier transform curves. Operando SR-FTIR measurements in the range of 600–4,000  $\text{cm}^{-1}$ , reproduced with permission<sup>[129]</sup>. Copyright 2021, Science Publishing Group; (B) The band position and peak intensity evolution of infrared signals assigned to  $\text{NiO}^*$  during OER, where the absorbance under the potential of 1.3 V is defined as “1” and absorbance under other potentials is plotted relative to that at 1.3 V, reproduced with permission<sup>[92]</sup>. Copyright 2021, Wiley-VCH; (C) Operando Raman spectra of FeNi DHBQ/NF, reproduced with permission<sup>[130]</sup>. Copyright 2023, Elsevier; (D) The *in situ* Raman spectra of Ni-MOFs NS along with CV test, reproduced with permission<sup>[131]</sup>. Copyright 2023, Elsevier. SR: Synchrotron-radiation; FTIR: Fourier transform infrared spectroscopy; OER: oxygen evolution reaction; DHBQ: dihydroxy-1,4-benzoquinone; NF: nickel foam; MOF: metal-organic framework; NS: nanoarrays; CV: cyclic voltammetry.

based on various characterization tools [Figure 19A] were simulated. To determine whether Ni or Fe sites were the active sites for oxygen electrocatalysis in  $\text{Ni}_{0.5}\text{Fe}_{0.5}\text{-THQ}$ , the theoretical adsorption energies of  $\text{OH}^-$  on the MOF surface were calculated [Figure 19B]. Then, the calculated Gibbs free energies of OER intermediates explored the potential limiting step for OER processes [Figure 19C]. The intrinsic electronic structures were analyzed using the density of states. It is evident that several electronic states exist around the Fermi level, guiding superior electrical conductivity and metalloid properties [Figure 19D]. Additionally, the  $d$ -band center ( $E_d$ ) reflects the absorption capacity of intermediates on the catalytic surface [Figure 19E]. Finally, by the calculated 3D differential charge density image, the electron transfer in the  $\text{Ni}_{0.5}\text{Fe}_{0.5}\text{-THQ}$  was gained [Figure 19F]. The results show that the Ni sites bearing more  $d$ -electrons can partially transfer their electrons to the Fe sites by the  $d$ - $\pi$  conjugation on the material surface. Additionally, it has been extensively demonstrated that the MOF undergoes *in situ* structural progress during the OER procedure due to strong electric field-driven MOF. DFT calculations show that the ad/desorption free energy of active sites was significantly optimized by the built-in electric field in the self-restructured MOF. Zhang *et al.* revealed a correlation between the MOF matrix and  $\text{NiOOH}$  via Operando EIS and DFT analysis<sup>[127]</sup>. Ding *et al.* presented an engineering strategy to improve the structural transformation of MOFs into metal oxyhydroxides during the OER process, resulting in increased activity<sup>[133]</sup>. MOFs with a high number of unsaturated metal sites are more likely to convert to metal oxyhydroxides than those without defects during OER. DFT calculations confirm that oxygen vacancies in metal-oxygen hydroxides boost the adsorptive strength of oxygenated intermediary compounds ( $\text{OH}^*$ ,  $\text{OOH}^*$ ,  $\text{O}^*$ ) in the active sites and thus increase the redox activity.



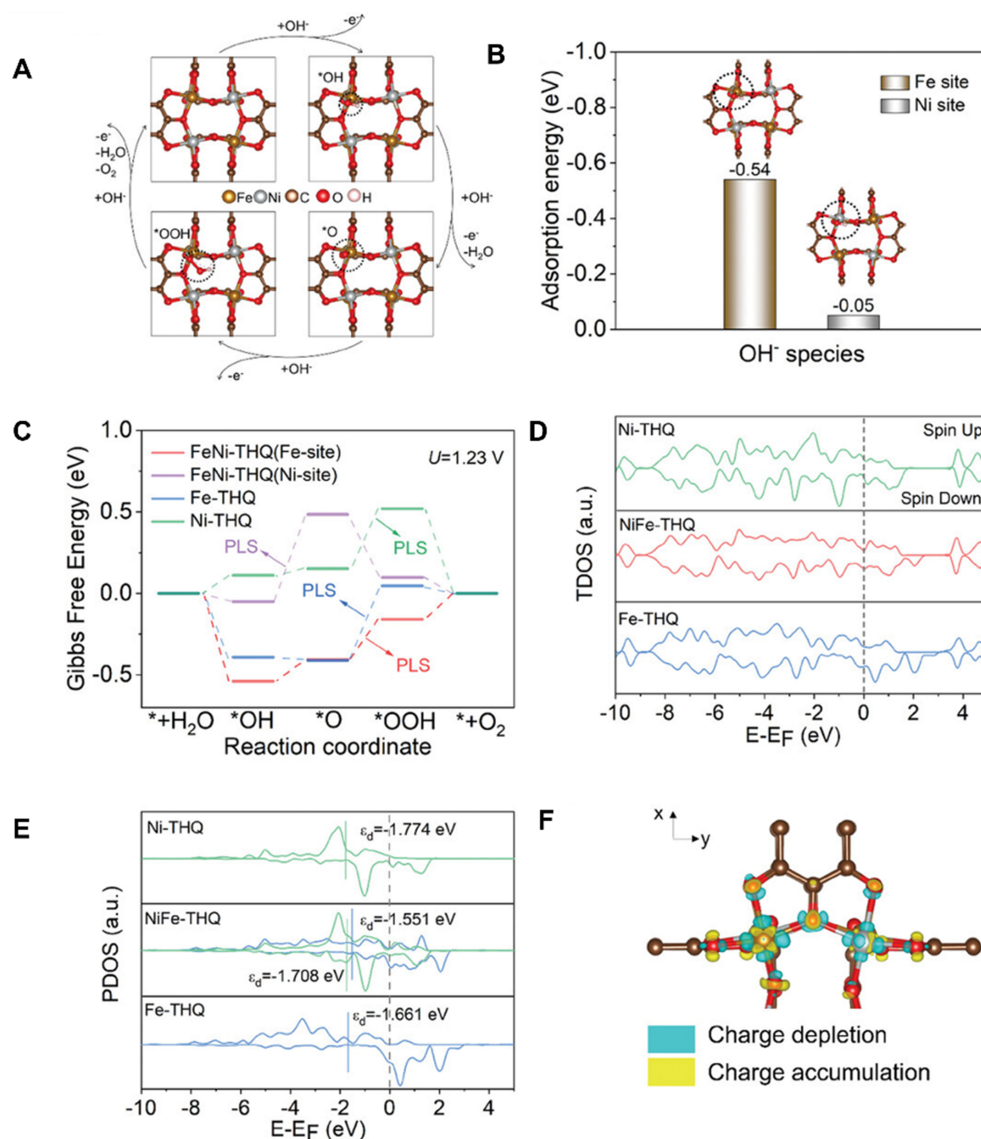


**Figure 19.** (A) Schematic illustration of the OER pathway for Ni<sub>0.5</sub>Fe<sub>0.5</sub>-THQ; (B) Adsorption energy of OH<sup>-</sup> on Fe and Ni sites in Ni<sub>0.5</sub>Fe<sub>0.5</sub>-THQ; (C) Free energy diagram for OER on Ni-THQ, NiFe-THQ (Fe-site or Ni site) and Fe-THQ; (D) TDOS and (E) PDOS diagrams of Ni-THQ, Ni<sub>0.5</sub>Fe<sub>0.5</sub>-THQ, and Fe-THQ; (F) The differential charge density image of Ni<sub>0.5</sub>Fe<sub>0.5</sub>-THQ, reproduced with permission<sup>[132]</sup>. Copyright 2021, Wiley-VCH. OER: Oxygen evolution reaction; THQ: tetrahydroxy-1,4-benzoquinone hydrate; TDOS: total density of states; PDOS: partial density of states.

## CONCLUSION AND OUTLOOK

Reasonable design and preparation of advanced OER electrocatalysts with high specific surface area, porous structure and ample exposed active sites is of great significance to developing metal-air cells, fuel cells and water electrolyzers. MOFs are considered as one of the most potential OER electrocatalysts due to their permanent porosity and rich active sites. However, most MOF electrocatalysts are powdery and require mixing with polymer binders and conductive additives to prepare working electrodes, which reduces their OER activity. Therefore, MOFs grown on the conductive substrate surface that can directly serve as working electrodes without additives are of great interest and high demand. We conclude that MOF-based self-supported electrodes have the following advantages: (1) Preparation methods of working electrodes are simple, and MOF aggregation can be avoided to effectively expose abundant active sites; (2) Direct growth

of MOFs on a conductive substrate can accelerate electron transfer between the active sites and collector; (3) Long-term electrocatalytic stability can be guaranteed by improving the adhesion between the electrocatalytic active substance and conductive substrate.

In this review, reasonable fabrication and optimization of MOF-based self-supported electrodes as excellent OER electrocatalysts were discussed in detail. Firstly, the OER mechanism under acidic and alkaline conditions and evaluation parameters of OER are introduced, including overpotential, faraday efficiency, TOF, electrochemical active area, Tafel slope, and stability. Then, the preparation strategies of MOF-based self-supported electrodes, such as *in situ* preparation strategy, semi-sacrificial template, full sacrificial template strategy, and electrochemical deposition, are systematically introduced. Then, we proposed a series of optimization strategies involved in mixed-metal nodes engineering, design of ligands and heterostructure engineering. In addition, post analysis and operando characterization technologies were discussed to fully understand the reaction mechanism during OER.

Although significant advances of MOF-based self-supported electrodes have been made in recent years, some pivotal matters and challenges remain to be further explored to exploit ideal energy conversion materials in OER. (1) During the OER process, MOFs undergo surface electronic structure reconstruction or even overall structural changes, which hinders their ability to fully utilize the advantages of their periodic lattice structure. It is important to note that even at low current densities, MOFs experience these changes due to the strong alkaline environment and the effect of the applied electric field. This reconstruction phenomenon complicates the study of the OER catalytic mechanism. Theoretical modeling and well-developed computational methods are powerful tools to gain insight into potential catalytic mechanisms. Still, the real role of MOFs and their derivatives in OER needs to be further clarified; (2) Although many studies have confirmed the involvement of LOM and OPM in the OER process, most current theoretical calculations on material activity are still based solely on AEM. This leads to unreliable predictions of catalyst performance and unreasonable probing of the source of activity; (3) Efficient oxygen evolution at high current density ( $> 500 \text{ mA}\cdot\text{cm}^{-2}$ ) requires a larger scale of charge and mass transfer and higher intrinsic activity of the active sites to allow for rapid reaction. This also demands higher conductivity and mass transfer capability of the MOF-based electrodes; (4) In addition to high performance, the cost of preparing MOF self-supported electrodes also needs to be considered. At present, most electrodes are based on foam metals and CC as a conductive substrate, stainless-steel mesh with lower prices, a simple preparation process and larger output can be widely used. Meanwhile, preparing MOF-based self-supported electrodes should also adopt more moderate synthesis routes to large-scale preparation of large-area electrodes for industrial demand; (5) At high current densities, numerous  $\text{H}_2$  bubbles cover the surface of working electrodes. This coverage significantly affects the exposed active sites, hinders charge and mass transfer, and makes it challenging to maintain long-lasting OER activity. Also, MOFs are easy to dissolve and fall off from the conductive substrate at high current density in aqueous solution, resulting in an obvious reduction in their activity and stability and limiting their long-term use; (6) The OER process of MOFs is usually carried out in alkaline media with fast reaction kinetics. However, it is desirable to replace the corrosive alkaline solution with a neutral medium. In addition, for the electrolytic water reaction, the other half of the reaction is fast under acidic conditions. Therefore, developing efficient and stable MOF-based self-supported electrodes at full pH is of great significance but remains a huge challenge.

Despite the remaining challenges, ongoing research on the application of MOF-based self-supported electrodes in OER and a deeper understanding of the reaction mechanism can provide valuable information to guide researchers in designing better electrodes. This, in turn, is expected to facilitate large-scale industrial applications. Here, we propose to explore some research directions in detail, as follows: (1) The



research involves using materials such as high valence metal-based MOFs, noble metal-based MOFs, and MOF complexes, including MOFs and conductive polymers, MOFs and two-dimensional conductive materials, and MOFs and covalent organic skeletal materials for catalyst research; (2) Elucidate the OER mechanism by combining *in situ* characterization, theoretical calculations and operando electrochemical methods; (3) Use the efficient catalytic electrodes from existing studies in actual electrolyzers to promote their catalytic performance.

## DECLARATIONS

### Authors' contributions

Prepared the manuscript: Li S

Corrected the manuscript: Tang D, Jing X

### Availability of data and materials

Not applicable.

### Financial support and sponsorship

We are grateful for the financial support from the National Natural Science Foundation of China (Grant Nos. 22131004 & U21A20330) and the “111” project (B18012). Tang D received support from the U.S. Department of Energy (DOE), Office of Basic Energy Sciences, Division of Chemical Sciences, Geosciences, and Biosciences under award DE-FG02-17ER16362.

### Conflicts of interest

All authors declared that there are no conflicts of interest.

### Ethical approval and consent to participate

Not applicable.

### Consent for publication

Not applicable.

### Copyright

© The Author(s) 2024.

## REFERENCES

1. Ball M, Weeda M. The hydrogen economy - Vision or reality? *Int J Hydrogen Energ* 2015;40:7903-19. [DOI](#)
2. Turner JA. Sustainable hydrogen production. *Science* 2004;305:972-4. [DOI](#) [PubMed](#)
3. Fleischmann S, Mitchell JB, Wang R, et al. Pseudocapacitance: from fundamental understanding to high power energy storage materials. *Chem Rev* 2020;120:6738-82. [DOI](#) [PubMed](#)
4. Xie H, Zhao Z, Liu T, et al. A membrane-based seawater electrolyser for hydrogen generation. *Nature* 2022;612:673-8. [DOI](#) [PubMed](#)
5. Zhang M, Liu Q, Sun W, et al. Nanostructured intermetallics: from rational synthesis to energy electrocatalysis. *Chem Synth* 2023;3:28. [DOI](#)
6. Xie X, Du L, Yan L, et al. Oxygen evolution reaction in alkaline environment: material challenges and solutions. *Adv Funct Mater* 2022;32:2110036. [DOI](#)
7. Liu W, Niu X, Tang J, et al. Energy-efficient anodic reactions for sustainable hydrogen production via water electrolysis. *Chem Synth* 2023;3:44. [DOI](#)
8. Suen NT, Hung SF, Quan Q, Zhang N, Xu YJ, Chen HM. Electrocatalysis for the oxygen evolution reaction: recent development and future perspectives. *Chem Soc Rev* 2017;46:337-65. [DOI](#) [PubMed](#)
9. Cui X, Ren P, Ma C, et al. Robust interface Ru centers for high-performance acidic oxygen evolution. *Adv Mater* 2020;32:e1908126. [DOI](#) [PubMed](#)
10. An L, Wei C, Lu M, et al. Recent development of oxygen evolution electrocatalysts in acidic environment. *Adv Mater*

- 2021;33:e2006328. DOI PubMed
11. Lee Y, Suntivich J, May KJ, Perry EE, Shao-Horn Y. Synthesis and activities of rutile IrO<sub>2</sub> and RuO<sub>2</sub> nanoparticles for oxygen evolution in acid and alkaline solutions. *J Phys Chem Lett* 2012;3:399-404. DOI PubMed
  12. McCrory CC, Jung S, Ferrer IM, Chatman SM, Peters JC, Jaramillo TF. Benchmarking hydrogen evolving reaction and oxygen evolving reaction electrocatalysts for solar water splitting devices. *J Am Chem Soc* 2015;137:4347-57. DOI PubMed
  13. Pei Y, Guo S, Ju Q, et al. Interface engineering with ultralow ruthenium loading for efficient water splitting. *ACS Appl Mater Interfaces* 2020;12:36177-85. DOI PubMed
  14. Zhao G, Li P, Cheng N, Dou SX, Sun W. An Ir/Ni(OH)<sub>2</sub> heterostructured electrocatalyst for the oxygen evolution reaction: breaking the scaling relation, stabilizing iridium(V), and beyond. *Adv Mater* 2020;32:e2000872. DOI PubMed
  15. Li H, Li G. Novel palladium-based nanomaterials for multifunctional ORR/OER/HER electrocatalysis. *J Mater Chem A* 2023;11:9383-400. DOI
  16. Trotochaud L, Ranney JK, Williams KN, Boettcher SW. Solution-cast metal oxide thin film electrocatalysts for oxygen evolution. *J Am Chem Soc* 2012;134:17253-61. DOI PubMed
  17. Vijayapradeep S, Kumar RS, Karthikeyan S, Ramakrishnan S, Yoo DJ. Constructing micro-nano rod-shaped iron-molybdenum oxide heterojunctions to enhance overall water electrolysis. *Mater Today Chem* 2024;36:101934. DOI
  18. Zhang B, Xiao C, Xie S, Liang J, Chen X, Tang Y. Iron-nickel nitride nanostructures in situ grown on surface-redox-etching nickel foam: efficient and ultrasustainable electrocatalysts for overall water splitting. *Chem Mater* 2016;28:6934-41. DOI
  19. Li H, Chen S, Zhang Y, et al. Systematic design of superaerophobic nanotube-array electrode comprised of transition-metal sulfides for overall water splitting. *Nat Commun* 2018;9:2452. DOI PubMed PMC
  20. Zhu Y, Liu Y, Ren T, Yuan Z. Self-supported cobalt phosphide mesoporous nanorod arrays: a flexible and bifunctional electrode for highly active electrocatalytic water reduction and oxidation. *Adv Funct Mater* 2015;25:7337-47. DOI
  21. Sai KNS, Tang Y, Dong L, Yu XY, Hong Z. N<sub>2</sub> plasma-activated NiO nanosheet arrays with enhanced water splitting performance. *Nanotechnology* 2020;31:455709. DOI PubMed
  22. Yang Q, Lu Z, Liu J, et al. Metal oxide and hydroxide nanoarrays: hydrothermal synthesis and applications as supercapacitors and nanocatalysts. *Prog Nat Sci Mater Int* 2013;23:351-66. DOI
  23. Hou J, Wu Y, Zhang B, Cao S, Li Z, Sun L. Rational design of nanoarray architectures for electrocatalytic water splitting. *Adv Funct Mater* 2019;29:1808367. DOI
  24. Zou X, Zhang Y. Noble metal-free hydrogen evolution catalysts for water splitting. *Chem Soc Rev* 2015;44:5148-80. DOI PubMed
  25. Qian Q, Li Y, Liu Y, Yu L, Zhang G. Ambient fast synthesis and active sites deciphering of hierarchical foam-like trimetal-organic framework nanostructures as a platform for highly efficient oxygen evolution electrocatalysis. *Adv Mater* 2019;31:e1901139. DOI PubMed
  26. Liu M, Kong L, Wang X, He J, Bu XH. Engineering bimetal synergistic electrocatalysts based on metal-organic frameworks for efficient oxygen evolution. *Small* 2019;15:e1903410. DOI PubMed
  27. Du J, Li F, Sun L. Metal-organic frameworks and their derivatives as electrocatalysts for the oxygen evolution reaction. *Chem Soc Rev* 2021;50:2663-95. DOI PubMed
  28. Tang Y, Lan Y. Rational design and synthesis of advanced metal-organic frameworks for electrocatalytic water splitting. *Sci China Chem* 2023;66:943-65. DOI
  29. Zhou C, Dong C, Wang W, et al. An ultrathin and crack-free metal-organic framework film for effective polysulfide inhibition in lithium-sulfur batteries. *Interdisciplinary Mater* 2024;3:306-15. DOI
  30. Lu XF, Liao PQ, Wang JW, et al. An alkaline-stable, metal hydroxide mimicking metal-organic framework for efficient electrocatalytic oxygen evolution. *J Am Chem Soc* 2016;138:8336-9. DOI PubMed
  31. Zhao S, Wang Y, Dong J, et al. Ultrathin metal-organic framework nanosheets for electrocatalytic oxygen evolution. *Nat Energy* 2016;1:16184. DOI
  32. Jiang Y, Chen TY, Chen JL, et al. Heterostructured bimetallic MOF-on-MOF architectures for efficient oxygen evolution reaction. *Adv Mater* 2024;36:e2306910. DOI PubMed
  33. Cheng W, Wu ZP, Luan D, Zang SQ, Lou XWD. Synergetic cobalt-copper-based bimetal-organic framework nanoboxes toward efficient electrochemical oxygen evolution. *Angew Chem Int Ed Engl* 2022;60:26397-402. DOI PubMed
  34. Zhu D, Liu J, Wang L, et al. A 2D metal-organic framework/Ni(OH)<sub>2</sub> heterostructure for an enhanced oxygen evolution reaction. *Nanoscale* 2019;11:3599-605. DOI PubMed
  35. Xu K, Chen P, Li X, et al. Metallic nickel nitride nanosheets realizing enhanced electrochemical water oxidation. *J Am Chem Soc* 2015;137:4119-25. DOI PubMed
  36. Iqbal S, Safdar B, Hussain I, Zhang K, Chatzichristodoulou C. Trends and prospects of bulk and single-atom catalysts for the oxygen evolution reaction. *Adv Energy Mater* 2023;13:2203913. DOI
  37. Yang H, Wang X, Hu Q, et al. Recent progress in self-supported catalysts for CO<sub>2</sub> electrochemical reduction. *Small Methods* 2020;4:1900826. DOI
  38. Zhang T, Sun J, Guan J. Self-supported transition metal chalcogenides for oxygen evolution. *Nano Res* 2023;16:8684-711. DOI
  39. Wang J, Jiang Y, Liu C, et al. In situ growth of hierarchical bimetal-organic frameworks on nickel-iron foam as robust electrodes for the electrocatalytic oxygen evolution reaction. *J Colloid Interface Sci* 2022;614:532-7. DOI PubMed
  40. Li FL, Shao Q, Huang X, Lang JP. Nanoscale trimetallic metal-organic frameworks enable efficient oxygen evolution

- electrocatalysis. *Angew Chem Int Ed Engl* 2018;57:1888-92. DOI PubMed
41. Duan J, Chen S, Zhao C. Ultrathin metal-organic framework array for efficient electrocatalytic water splitting. *Nat Commun* 2017;8:15341. DOI PubMed PMC
42. Zhao X, Tao K, Han L. Self-supported metal-organic framework-based nanostructures as binder-free electrodes for supercapacitors. *Nanoscale* 2022;14:2155-66. DOI PubMed
43. Zhang X, Jin M, Jia F, et al. Noble-metal-free oxygen evolution reaction electrocatalysts working at high current densities over 1000 mA cm<sup>-2</sup>: from fundamental understanding to design principles. *Energy Environ Mater* 2023;6:e12457. DOI
44. Goswami A, Ghosh D, Pradhan D, Biradha K. In situ grown Mn(II) MOF upon nickel foam acts as a robust self-supporting bifunctional electrode for overall water splitting: a bimetallic synergistic collaboration strategy. *ACS Appl Mater Interfaces* 2022;14:29722-34. DOI PubMed
45. Wang Y, Yan L, Dastafkan K, et al. Lattice matching growth of conductive hierarchical porous MOF/LDH heteronanotube arrays for highly efficient water oxidation. *Adv Mater* 2021;33:e2006351. DOI PubMed
46. Jiao L, Wei W, Li X, et al. Value-added formate production from selective ethylene glycol oxidation based on cost-effective self-supported MOF nanosheet arrays. *Rare Met* 2022;41:3654-61. DOI
47. Zhong L, He L, Wang N, et al. Preparation of metal-organic framework from in situ self-sacrificial stainless-steel matrix for efficient water oxidation. *Appl Catal B Environ* 2023;325:122343. DOI
48. Luo Y, Zhang Z, Chhowalla M, Liu B. Recent advances in design of electrocatalysts for high-current-density water splitting. *Adv Mater* 2022;34:e2108133. DOI PubMed
49. Wang Z, Xu J, Yang J, Xue Y, Dai L. Ultraviolet/ozone treatment for boosting OER activity of MOF nanoneedle arrays. *Chem Eng J* 2022;427:131498. DOI
50. Wang Y, Liu B, Shen X, et al. Engineering the activity and stability of MOF-nanocomposites for efficient water oxidation. *Adv Energy Mater* 2021;11:2003759. DOI
51. Zhang B, Zheng Y, Ma T, et al. Designing MOF nanoarchitectures for electrochemical water splitting. *Adv Mater* 2021;33:e2006042. DOI PubMed
52. Liang Q, Chen J, Wang F, Li Y. Transition metal-based metal-organic frameworks for oxygen evolution reaction. *Coord Chem Rev* 2020;424:213488. DOI
53. Wang X, Zhou W, Zhai S, et al. Metal-organic frameworks: direct synthesis by organic acid-etching and reconstruction disclosure as oxygen evolution electrocatalysts. *Angew Chem Int Ed Engl* 2024;63:e202400323. DOI PubMed
54. Li S, Wang Z, Wang T, et al. Preparation of trimetallic-organic framework film electrodes via secondary growth for efficient oxygen evolution reaction. *Chemistry* 2023;29:e202301129. DOI PubMed
55. Jiang S, Suo H, Zheng X, et al. Lightest metal leads to big change: lithium-mediated metal oxides for oxygen evolution reaction. *Adv Energy Mater* 2022;12:2201934. DOI
56. Wang N, Ou P, Miao RK, et al. Doping shortens the metal/metal distance and promotes OH coverage in non-noble acidic oxygen evolution reaction catalysts. *J Am Chem Soc* 2023;145:7829-36. DOI PubMed
57. Lin C, Li J, Li X, et al. In-situ reconstructed Ru atom array on  $\alpha$ -MnO<sub>2</sub> with enhanced performance for acidic water oxidation. *Nat Catal* 2021;4:1012-23. DOI
58. Xu S, Feng S, Yu Y, et al. Dual-site segmentally synergistic catalysis mechanism: boosting CoFeS<sub>x</sub> nanocluster for sustainable water oxidation. *Nat Commun* 2024;15:1720. DOI PubMed PMC
59. Liu D, Xu W, Liu Q, et al. Unsaturated-sulfur-rich MoS<sub>2</sub> nanosheets decorated on free-standing SWNT film: synthesis, characterization and electrocatalytic application. *Nano Res* 2016;9:2079-87. DOI
60. You B, Jiang N, Sheng M, Bhushan MW, Sun Y. Hierarchically porous urchin-like Ni<sub>3</sub>P superstructures supported on nickel foam as efficient bifunctional electrocatalysts for overall water splitting. *ACS Catal* 2016;6:714-21. DOI
61. Liang H, Gandhi AN, Anjum DH, Wang X, Schwingenschlögl U, Alshareef HN. Plasma-assisted synthesis of NiCoP for efficient overall water splitting. *Nano Lett* 2016;16:7718-25. DOI PubMed
62. Görlin M, Chernev P, Ferreira de Araújo J, et al. Oxygen evolution reaction dynamics, faradaic charge efficiency, and the active metal redox states of Ni-Fe oxide water splitting electrocatalysts. *J Am Chem Soc* 2016;138:5603-14. DOI PubMed
63. Liu Y, Ying Y, Fei L, et al. Valence engineering via selective atomic substitution on tetrahedral sites in spinel oxide for highly enhanced oxygen evolution catalysis. *J Am Chem Soc* 2019;141:8136-45. DOI PubMed
64. Li S, Xiao Y, Yan H, et al. Ultrafine platinum nanoparticles anchored in porous aromatic frameworks for efficient hydrogen evolution reaction. *Chem Commun* 2023;59:4766-9. DOI PubMed
65. Pan C, Liu Z, Huang M. 2D iron-doped nickel MOF nanosheets grown on nickel foam for highly efficient oxygen evolution reaction. *Appl Surf Sci* 2020;529:147201. DOI
66. Zhou W, Xue Z, Liu Q, Li Y, Hu J, Li G. Trimetallic MOF-74 films grown on Ni foam as bifunctional electrocatalysts for overall water splitting. *ChemSusChem* 2020;13:5647-53. DOI PubMed
67. Liu Q, Xie L, Shi X, et al. High-performance water oxidation electrocatalysis enabled by a Ni-MOF nanosheet array. *Inorg Chem Front* 2018;5:1570-4. DOI
68. Chen J, Ren B, Cui H, Wang C. Constructing pure phase tungsten-based bimetallic carbide nanosheet as an efficient bifunctional electrocatalyst for overall water splitting. *Small* 2020;16:e1907556. DOI PubMed
69. Hong Q, Wang Y, Wang R, et al. In situ coupling of carbon dots with Co-ZIF nanoarrays enabling highly efficient oxygen evolution

- electrocatalysis. *Small* 2023;19:e2206723. DOI PubMed
70. Xu Z, Yeh CL, Jiang Y, et al. Orientation-adjustable metal-organic framework nanorods for efficient oxygen evolution reaction. *ACS Appl Mater Interfaces* 2021;13:28242-51. DOI PubMed
71. Huang L, Gao G, Zhang H, Chen J, Fang Y, Dong S. Self-dissociation-assembly of ultrathin metal-organic framework nanosheet arrays for efficient oxygen evolution. *Nano Energy* 2020;68:104296. DOI
72. Raja D, Chuah X, Lu S. In situ grown bimetallic MOF-based composite as highly efficient bifunctional electrocatalyst for overall water splitting with ultrastability at high current densities. *Adv Energy Mater* 2018;8:1801065. DOI
73. Wang C, Feng Y, Sun H, et al. Self-optimized metal-organic framework electrocatalysts with structural stability and high current tolerance for water oxidation. *ACS Catal* 2021;11:7132-43. DOI
74. Li D, Li Q, Gu Z, Zhang J. A surface-mounted MOF thin film with oriented nanosheet arrays for enhancing the oxygen evolution reaction. *J Mater Chem A* 2019;7:18519-28. DOI
75. Cai G, Zhang W, Jiao L, Yu S, Jiang H. Template-directed growth of well-aligned MOF arrays and derived self-supporting electrodes for water splitting. *Chem* 2017;2:791-802. DOI
76. Li W, Watzele S, El-Sayed HA, et al. Unprecedented high oxygen evolution activity of electrocatalysts derived from surface-mounted metal-organic frameworks. *J Am Chem Soc* 2019;141:5926-33. DOI PubMed
77. Li H, Du Z, He F, Chen S, Yang H, Tang K. Cobalt carbonate hydroxide assisted formation of self-supported CoNi-based metal-organic framework nanostrips as efficient electrocatalysts for oxygen evolution reaction. *Int J Hydrogen Energ* 2023;48:15566-73. DOI
78. Cao C, Ma D, Xu Q, Wu X, Zhu Q. Semisacrificial template growth of self-supporting MOF nanocomposite electrode for efficient electrocatalytic water oxidation. *Adv Funct Mater* 2019;29:1807418. DOI
79. Zheng F, Zhang W, Zhang X, Zhang Y, Chen W. Sub-2 nm ultrathin and robust 2D FeNi layered double hydroxide nanosheets packed with 1D FeNi-MOFs for enhanced oxygen evolution electrocatalysis. *Adv Funct Mater* 2021;31:2103318. DOI
80. Li S, Wang T, Tang D, et al. Metal-organic framework integrating ionic framework and bimetallic coupling effect for highly efficient oxygen evolution reaction. *Adv Sci* 2022;9:e2203712. DOI PubMed PMC
81. Li S, Zeng S, Tian Y, Jing X, Sun F, Zhu G. Two flexible cationic metal-organic frameworks with remarkable stability for CO<sub>2</sub>/CH<sub>4</sub> separation. *Nano Res* 2021;14:3288-93. DOI
82. Cheng W, Lu XF, Luan D, Lou XWD. NiMn-based bimetal-organic framework nanosheets supported on multi-channel carbon fibers for efficient oxygen electrocatalysis. *Angew Chem Int Ed Engl* 2020;59:18234-9. DOI PubMed
83. Babu A, Varghese A. Electrochemical deposition for metal organic frameworks: advanced energy, catalysis, sensing and separation applications. *J Electroanal Chem* 2023;937:117417. DOI
84. Zhang X, Wan K, Subramanian P, Xu M, Luo J, Fransaeer J. Electrochemical deposition of metal-organic framework films and their applications. *J Mater Chem A* 2020;8:7569-87. DOI
85. Varsha MV, Nageswaran G. Review - direct electrochemical synthesis of metal organic frameworks. *J Electrochem Soc* 2020;167:155527. DOI
86. Guo Y, Zhang C, Zhang J, et al. Metal-organic framework-derived bimetallic NiFe selenide electrocatalysts with multiple phases for efficient oxygen evolution reaction. *ACS Sustain Chem Eng* 2021;9:2047-56. DOI
87. Wang L, Wu Y, Cao R, et al. Fe/Ni metal-organic frameworks and their binder-free thin films for efficient oxygen evolution with low overpotential. *ACS Appl Mater Interfaces* 2016;8:16736-43. DOI PubMed
88. Shahbazi Farahani F, Rahmanifar MS, Noori A, et al. Correction to "Trilayer metal-organic frameworks as multifunctional electrocatalysts for energy conversion and storage applications". *J Am Chem Soc* 2022;144:15903-6. DOI PubMed
89. Lyu S, Guo C, Wang J, et al. Exceptional catalytic activity of oxygen evolution reaction via two-dimensional graphene multilayer confined metal-organic frameworks. *Nat Commun* 2022;13:6171. DOI PubMed PMC
90. Du J, Xu S, Sun L, Li F. Iron carbonate hydroxide templated binary metal-organic frameworks for highly efficient electrochemical water oxidation. *Chem Commun* 2019;55:14773-6. DOI PubMed
91. Lin H, Senthil Raja D, Chuah X, Hsieh C, Chen Y, Lu S. Bi-metallic MOFs possessing hierarchical synergistic effects as high performance electrocatalysts for overall water splitting at high current densities. *Appl Catal B Environ* 2019;258:118023. DOI
92. Sun X, Zhang X, Li Y, et al. In situ construction of flexible V-Ni redox centers over Ni-based MOF nanosheet arrays for electrochemical water oxidation. *Small Methods* 2021;5:e2100573. DOI PubMed
93. Li Y, Wu Y, Li T, et al. Tuning the electronic structure of a metal-organic framework for an efficient oxygen evolution reaction by introducing minor atomically dispersed ruthenium. *Carbon Energy* 2023;5:e265. DOI
94. Wu J, Yu Z, Zhang Y, et al. Understanding the effect of second metal on CoM (M = Ni, Cu, Zn) metal-organic frameworks for electrocatalytic oxygen evolution reaction. *Small* 2021;17:e2105150. DOI PubMed
95. Raja D, Huang C, Chen Y, Choi Y, Lu S. Composition-balanced trimetallic MOFs as ultra-efficient electrocatalysts for oxygen evolution reaction at high current densities. *Appl Catal B Environ* 2020;279:119375. DOI
96. Jiang W, Wang J, Jiang Y, et al. Multivalent ruthenium immobilized by self-supported NiFe-organic frameworks for efficient electrocatalytic overall water splitting. *J Mater Chem A* 2023;11:2769-79. DOI
97. Zhao M, Li H, Li W, et al. Ru-doping enhanced electrocatalysis of metal-organic framework nanosheets toward overall water splitting. *Chemistry* 2020;26:17091-6. DOI PubMed
98. Zhang R, Ren X, Hao S, et al. Selective phosphidation: an effective strategy toward CoP/CeO<sub>2</sub> interface engineering for superior



- alkaline hydrogen evolution electrocatalysis. *J Mater Chem A* 2018;6:1985-90. DOI
99. Li F, Jiang M, Lai C, Xu H, Zhang K, Jin Z. Yttrium- and cerium-codoped ultrathin metal-organic framework nanosheet arrays for high-efficiency electrocatalytic overall water splitting. *Nano Lett* 2022;22:7238-45. DOI PubMed
100. Yao N, Jia H, Fan Z, et al. Nitridation-induced metal-organic framework nanosheet for enhanced water oxidation electrocatalysis. *J Energy Chem* 2022;64:531-7. DOI
101. Liu Y, Li X, Zhang S, et al. Molecular engineering of metal-organic frameworks as efficient electrochemical catalysts for water oxidation. *Adv Mater* 2023;35:e2300945. DOI PubMed
102. Xue Z, Liu K, Liu Q, et al. Missing-linker metal-organic frameworks for oxygen evolution reaction. *Nat Commun* 2019;10:5048. DOI PubMed PMC
103. Ji Q, Kong Y, Wang C, et al. Lattice strain induced by linker scission in metal-organic framework nanosheets for oxygen evolution reaction. *ACS Catal* 2020;10:5691-7. DOI
104. Cheng W, Zhao X, Su H, et al. Lattice-strained metal-organic-framework arrays for bifunctional oxygen electrocatalysis. *Nat Energy* 2019;4:115-22. DOI
105. Xu H, Fei B, Cai G, et al. Boronization-induced ultrathin 2D nanosheets with abundant crystalline-amorphous phase boundary supported on nickel foam toward efficient water splitting. *Adv Energy Mater* 2020;10:1902714. DOI
106. Zhai Q, Hu KJ, Shi Y, et al. Amorphous metal-organic framework-derived electrocatalyst to boost water oxidation. *J Phys Chem Lett* 2023;14:1156-64. DOI PubMed
107. Li Y, Wu Y, Li T, et al. Amorphous engineering of scalable metal-organic framework-derived electrocatalyst for highly efficient oxygen evolution reaction. *Small* 2024:e2311356. DOI PubMed
108. Li Z, Hu M, Wang P, Liu J, Yao J, Li C. Heterojunction catalyst in electrocatalytic water splitting. *Coord Chem Rev* 2021;439:213953. DOI
109. Deng L, Hu F, Ma M, et al. Electronic modulation caused by interfacial Ni-O-M (M= Ru, Ir, Pd) bonding for accelerating hydrogen evolution kinetics. *Angew Chem Int Ed Engl* 2021;60:22276-82. DOI PubMed
110. Yang J, Shen Y, Sun Y, Xian J, Long Y, Li G. Ir nanoparticles anchored on metal-organic frameworks for efficient overall water splitting under pH-universal conditions. *Angew Chem Int Ed Engl* 2023;62:e202302220. DOI PubMed
111. Cheng C, Cheng P, Huang C, Senthil Raja D, Wu Y, Lu S. Gold nanocrystal decorated trimetallic metal organic frameworks as high performance electrocatalysts for oxygen evolution reaction. *Appl Catal B Environ* 2021;286:119916. DOI
112. Zhang W, Hu Q, Wang L, et al. In-situ generated Ni-MOF/LDH heterostructures with abundant phase interfaces for enhanced oxygen evolution reaction. *Appl Catal B Environ* 2021;286:119906. DOI
113. Wei X, Li N, Liu N. Ultrathin NiFeZn-MOF nanosheets containing few metal oxide nanoparticles grown on nickel foam for efficient oxygen evolution reaction of electrocatalytic water splitting. *Electrochim Acta* 2019;318:957-65. DOI
114. Li W, Zhang H, Zhang K, et al. Altered electronic structure of trimetallic FeNiCo-MOF nanosheets for efficient oxygen evolution. *Chem Commun* 2023;59:4750-3. DOI PubMed
115. Xu J, Zhao Y, Li M, Fan G, Yang L, Li F. A strong coupled 2D metal-organic framework and ternary layered double hydroxide hierarchical nanocomposite as an excellent electrocatalyst for the oxygen evolution reaction. *Electrochim Acta* 2019;307:275-84. DOI
116. Kung CW, Mondloch JE, Wang TC, et al. Metal-organic framework thin films as platforms for atomic layer deposition of cobalt ions to enable electrocatalytic water oxidation. *ACS Appl Mater Interfaces* 2015;7:28223-30. DOI PubMed
117. Li CF, Xie LJ, Zhao JW, et al. Interfacial Fe-O-Ni-O-Fe bonding regulates the active Ni sites of Ni-MOFs via iron doping and decorating with FeOOH for super-efficient oxygen evolution. *Angew Chem Int Ed Engl* 2022;61:e202116934. DOI PubMed
118. Ni C, Zheng H, Liu W, et al. Linker defects in metal-organic frameworks for the construction of interfacial dual metal sites with high oxygen evolution activity. *Adv Funct Mater* 2023;33:2301075. DOI
119. Qian Z, Wang K, Shi K, et al. Interfacial electron transfer of heterostructured MIL-88A/Ni(OH)<sub>2</sub> enhances the oxygen evolution reaction in alkaline solutions. *J Mater Chem A* 2020;8:3311-21. DOI
120. Wu F, Guo X, Hao G, Hu Y, Jiang W. Electrodeposition of sulfur-engineered amorphous nickel hydroxides on MIL-53(Fe) nanosheets to accelerate the oxygen evolution reaction. *Nanoscale* 2019;11:14785-92. DOI PubMed
121. Mu G, Wang G, Huang Q, et al. A kinetic control strategy for one-pot synthesis of efficient bimetallic metal-organic framework/layered double hydroxide heterojunction oxygen evolution electrocatalysts. *Adv Funct Mater* 2023;33:2211260. DOI
122. Xiao M, Wu C, Zhu J, et al. In situ generated layered NiFe-LDH/MOF heterostructure nanosheet arrays with abundant defects for efficient alkaline and seawater oxidation. *Nano Res* 2023;16:8945-52. DOI
123. Ye L, Zhang Y, Zhang M, Gong Y. An ingeniously assembled metal-organic framework on the surface of FeMn co-doped Ni(OH)<sub>2</sub> as a high-efficiency electrocatalyst for the oxygen evolution reaction. *Dalton Trans* 2021;50:11775-82. DOI PubMed
124. Zheng W, Liu M, Lee LYS. Electrochemical instability of metal-organic frameworks: in situ spectroelectrochemical investigation of the real active sites. *ACS Catal* 2020;10:81-92. DOI
125. Zhong H, Zhang Q, Yu J, et al. Fundamental understanding of structural reconstruction behaviors in oxygen evolution reaction electrocatalysts. *Adv Energy Mater* 2023;13:2301391. DOI
126. Zheng W, Lee LYS. Metal-organic frameworks for electrocatalysis: catalyst or precatalyst? *ACS Energy Lett* 2021;6:2838-43. DOI
127. Zhang L, Wang J, Jiang K, et al. Self-reconstructed metal-organic framework heterojunction for switchable oxygen evolution reaction. *Angew Chem Int Ed Engl* 2022;61:e202214794. DOI PubMed

128. Kandambeth S, Kale VS, Fan D, et al. Unveiling chemically robust bimetallic squarate-based metal–organic frameworks for electrocatalytic oxygen evolution reaction. *Adv Energy Mater* 2023;13:2202964. [DOI](#)
129. Cheng W, Xi S, Wu ZP, Luan D, Lou XW. In situ activation of Br-confined Ni-based metal-organic framework hollow prisms toward efficient electrochemical oxygen evolution. *Sci Adv* 2021;7:eabk0919. [DOI](#) [PubMed](#) [PMC](#)
130. Liu J, Yu Z, Huang J, et al. Redox-active ligands enhance oxygen evolution reaction activity: regulating the spin state of ferric ions and accelerating electron transfer. *J Colloid Interface Sci* 2023;650:1182-92. [DOI](#) [PubMed](#)
131. Dai L, Fang C, Yao F, et al. Thickness-dependent  $\beta/\gamma$ -NiOOH transformation of Ni-MOFs in oxygen evolution reaction. *Appl Surf Sci* 2023;623:156991. [DOI](#)
132. Zhao L, Yan J, Huang H, et al. Regulating electronic structure of bimetallic NiFe-THQ conductive metal–organic frameworks to boost catalytic activity for oxygen evolution reaction. *Adv Funct Mater* 2024;34:2310902. [DOI](#)
133. Ding J, Guo D, Wang N, et al. Defect engineered metal-organic framework with accelerated structural transformation for efficient oxygen evolution reaction. *Angew Chem Int Ed Engl* 2023;62:e202311909. [DOI](#) [PubMed](#)